Penetrator Resistance and Target Damage due to Multiple Impacts Upon Granite and Concrete:

FINAL REPORT

Submitted To:
Major Michael Chipley
Program Director, Particulate Mechanics
Air Force Office of Scientific Research
Bolling Air Force Base, Washington D.C. 20332-6448

Submitted By:
Arun Shukla, Martin H. Sadd,

20000703 019

Department of Mechanical Engineering & Applied Mechanics
University of Rhode Island, Kingston, RI 02881

May 2000

REPORT DOCUMENTATION PAGE

AFRL-SR-BL-TR-00-

0247

1. REPORT DATE (DD-MM-YYYY) 24-05-2000	2. REPORT TYPE Final Report	3. DATES COVERED (From - To) 01-1998 to 05-2000

4. TITLE AND SUBTITLE	5a. CONTRACT NUMBER
Pentrator Resistance and Target Damage due to Multiple Impacts Upon Granite and Concrete	F496209810123
	5b. GRANT NUMBER
	5c. PROGRAM ELEMENT NUMBER

6. AUTHOR(S)	5d. PROJECT NUMBER
Arun Shukla	
Martin Sadd	5e. TASK NUMBER
	5f. WORK UNIT NUMBER

7. PERFORMING ORGANIZATION NAME(S) AND ADDRESS(ES)	8. PERFORMING ORGANIZATION REPORT NUMBER
Department of Mechanical Engineering and Applied Mechanics University of Rhode Island Kingston, RI 02881	AFSOR 99

9. SPONSORING / MONITORING AGENCY NAME(S) AND ADDRESS(ES)	10. SPONSOR/MONITOR'S ACRONYM(S)
Air Force Office of Scientific Research Particulate Mechanics Program Bolling Air Force Base Washington, DC 20332	
	11. SPONSOR/MONITOR'S REPORT NUMBER(S)

12. DISTRIBUTION / AVAILABILITY STATEMENT
Approved for Public Release: Distribution is unlimited

13. SUPPLEMENTARY NOTES

14. ABSTRACT
The objectives of this work were to develop first principle-based understanding of multiple impact, penetration, and damage accumulation in granite and concrete, and to develop a predictive model for multiple impact penetration. The extensive use of granite and concrete in military applications provides motivation for this work.

In order to understand the penetration process of granite and concrete dynamic and static material properties were determined as a function of induced damage. Quasi-static compression and tensile splitting experiments were conducted per ASTM Standards. Both the concrete and granite displayed a decrease in compressive strength as the damaged was increased. However, for the tensile splitting experiments it was found that the strength was highly dependent on the crack orientation. Dynamically the materials showed no decrease in compressive strength with increased damaged. The dynamic tensile strength of the materials did decrease with damage however they did not show the same orientation dependence as the static splitting strength.

A series of multiple impact experiments were performed on both concrete and granite using ogive nose projectile made of maraging steel. An existing model, developed by M. Forrestal, was used to predict the single impact penetration into concrete. In order to predict the penetration of subsequent impacts, the model was modified to account for the material property changes as a function of damage induced by the previous impacts. The empirically based model agreed well with the experimental data.

15. SUBJECT TERMS
Impact, Granite, Concrete, Projectile, Damage, Static Strength, Dynamic Strength.

16. SECURITY CLASSIFICATION OF: Unclassified			17. LIMITATION OF ABSTRACT	18. NUMBER OF PAGES	19a. NAME OF RESPONSIBLE PERSON
a. REPORT	b. ABSTRACT	c. THIS PAGE	SAR		19b. TELEPHONE NUMBER (include area code)

Standard Form 298 (Rev. 8-98)
Prescribed by ANSI Std. Z39.18

ABSTRACT

The objectives of this work were to develop first principle-based understanding of multiple impact, penetration, and damage accumulation in granite and concrete, and to develop a predictive model for multiple impact penetration. The extensive use of granite and concrete in military applications provides motivation for this work.

In order to understand the penetration process of granite and concrete dynamic and static material properties were determined as a function of induced damage. Quasi-static compression and tensile splitting experiments were conducted per ASTM Standards. Both the concrete and granite displayed a decrease in compressive strength as the damaged was increased. However, for the tensile splitting experiments it was found that the strength was highly dependent on the crack orientation. Dynamically the materials showed no decrease in compressive strength with increased damaged. The dynamic tensile strength of the materials did decrease with damage however they did not show the same orientation dependence as the static splitting strength.

A series of multiple impact experiments were performed on both concrete and granite using ogive nose projectile made of maraging steel. An existing model, developed by M. Forrestal, was used to predict the single impact penetration into concrete. In order to predict the penetration of subsequent impacts, the model was modified to account for the material property changes as a function of damage induced by the previous impacts. The empirically based model agreed well with the experimental data.

TABLE OF CONTENTS

CHAPTER 1   STATIC AND DYNAMIC BEHAVIOR OF CONCRETE AND GRANITE IN COMPRESSION WITH INDUCED DAMAGE

1.1 INTRODUCTION

Geological materials such as rock and concrete inherently contain a large number of defects or microcracks. Voids, inhomogeneities, and soft minerals in contact with stiff matrix materials all represent defects. Each defect gives rise to a stress concentration and reduces the strength of the local zone. These microcracks will eventually lead to structural failure under increasing load. An increment of the external static or dynamic load acting on the rock can cause local rupture of a certain fraction of weak zones leading to macroscopic deformation of the material. Prior to the formation of major cracks in rock, the rupture of local weak zones sharply increases with the loading force until a fracture appears throughout the whole rock. This process can be described by *continuous damage mechanics theory*, which states that rock is damaged by micro-fractures continuously from the initial stage of low stress to the end stage in which fracture occurs. It is believed that there must be a strong link between the rock damage and its constitutive behavior as reflected in its stress-strain response.

Several researchers have developed models to describe the stress-strain behavior of rock. Relatively early work includes the contribution of Weibull [11], who formulated a simple distribution law based on elementary statistical theory and postulated the Weibull three parameter tensile strength distribution. Other work includes Hudson and Fairhurst [12], using the idea of rock damage in terms of a *survival fraction*. The simple structure-disintegration model enables a form of the stress-strain curve for a specimen to

be synthesized from a qualitative knowledge of the local strain and local strength variation within the specimen. An active damage model for a specimen in uniaxial tension was developed by Krajcinovic and Silva [13]. Similar work was conducted by Weber and Saint-Lot [14]. Wiederhorn [15] first presented a theory in which the applied stress and rock strength were expressed in terms of probability functions which indicated the likelihood that the applied stress and rock strength are within prescribed limits. If the applied stress and rock strength are known with some degree of certainty, the probability of fracture of the rock mass can be determined. Tang [16] investigated the behavior of rock during compression failure based on the progressive development of axial microcracks. Various researchers have observed the statistical phenomenon caused by a distribution of microcracks over the volume of the material (Jaeger and Cook [17]; Swan, [18];Ratigan, [19]; Medrano and Gillis , [20];) The most commonly used probability distribution functions are the negative exponential (Priest and Hudson, [21];), the normal (Priest and Hudson, [22]), the lognormal (Sen and Kazi, [23]) , the gamma (Sen and Kazi, [24]) and the Weibull (Rouleau, [25]; Bardsley, [26]). The previous work studied the distribution of defects and material strength, but did not establish a relationship between stress and strain.

The present work presents an experimental and theoretical study of the stress-strain behavior of Barre granite and G mix concrete in compression, which was subjected to incremental prior damage. The experimental work involves the compression testing of cylindrical specimens which have had induced damage through a drop weight impact device. The input damage energy was correlated with the changes in the measured stress-

2

strain response. A statistical model was developed to simulate this behavior. Model results correlate reasonably well with experimental data.

1.2 PROPOSED MODEL FOR GRANITE

Starting with the basic concept from damage mechanics, the following uniaxial stress-strain law is proposed

$$\sigma = E(1-D)\varepsilon \qquad (1)$$

where σ is the stress, ε is the strain, E is Young's modulus , and D is the damage parameter ($0 \leq D \leq 1$) with $D = 0$ for undamaged material. The quantity (1 - D) can be thought of as the relative area capable of carrying the internal forces. Therefore, (1 - D) represents the ratio of the equivalent force-resistant area S_{eq} to the total cross-sectional area S_T, i.e.

$$1-D = \frac{S_{eq}}{S_T} \qquad (2)$$

Since S_T-S_{eq} denotes the area of the damaged section, it can been seen that D represents the internal damage of the material, and from relation (2), it follows that

$$D = 1-\frac{S_{eq}}{S_T} = \frac{S_T - S_{eq}}{S_T} \qquad (3)$$

Because rock damage is normally irreversible, D is a monotonically increasing function of load. In order to obtain the stress-strain relation of rock, the damage parameter D should first be found.

For a uniaxial compression specimen, we can divide the specimen cross-section into many small local area elements as shown in Figure 1. Because one element has a

different number of defects from another, these elements would show different failure strengths.
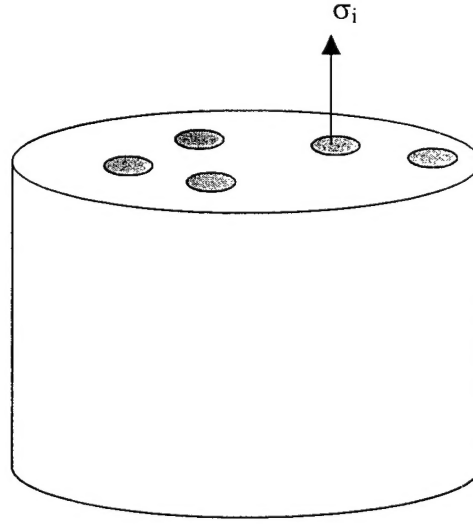
Figure 1. Schematic of Damage Concept

It is therefore assumed that local element strain strengths, ε_s, are distributed as a probability function. The strain ε is progressively increased with applied load on the specimen, and some elements fail locally when ε exceeds its strength ε_s, i. e. $\varepsilon \geq \varepsilon_s$. The study by Sen [24], indicates that a Weibull probability distribution function can be used to describe the intact lengths along a scanline of rock. Using these ideas, one assumption is that, even though the macroscopic behavior of the rock material is nonlinear, each element of the specimen is a Hookean material and follows the law

$$\sigma_i = E_i e_i \quad (i = 1,2,3,...) \qquad (4)$$

where E_i is the Young's modulus of the ith element. Additionally, it is assumed that the strength of the local elements follow Weibull's distribution density

$$\Phi(\varepsilon_s) = \frac{m}{\varepsilon_0}\left(\frac{\varepsilon_s}{\varepsilon_0}\right)^{m-1} e^{-\left(\frac{\varepsilon_s}{\varepsilon_0}\right)^m} \qquad (5)$$

where ε_s is the strength of the individual element, m is a shape parameter related to rock damage, and ε_0 is a measure of the average strain.

The proportion of damaged elements is equivalent to the probability for $\varepsilon > \varepsilon_s$. Therefore the damage area in the cross-section of the rock specimen is given by

$$S_T - S_{eq} = S_T \int_0^\varepsilon \Phi(x)dx \qquad (6)$$

Substituting equations (5) and (6) into (3), we obtain the following expression for the damage parameter D,

$$D = \int_0^\varepsilon \Phi(x)dx = 1 - e^{-\left(\frac{\varepsilon}{\varepsilon_0}\right)^m} \qquad (7)$$

Combining equation (7) and (1), the damage constitutive relation of rock under uniaxial compression is thus given by

$$\sigma = E\varepsilon\, e^{-\left(\frac{\varepsilon}{\varepsilon_0}\right)^m} \qquad (8)$$

1.3 COMPRESSION TESTING OF GRANITE

Cylindrical granite specimens (height = 31mm, diameter = 50mm) were chosen for the experimental program. The specific material was Regal Grey Granite (quarried in Barre, Vermont) which was selected because of its fine, uniform microstructure. Some physical properties of this granite are: compressive strength = 216.5 MPa, modulus of rupture = 180 kPa and density = 2.638 g/cm^3. Before compression testing, specimens were subjected to input damage from a drop weight testing apparatus. The free-drop impact setup is illustrated in Figure 2. It consists of a 2.015kg cylindrical steel projectile

that slides in a 50mm diameter PVC pipe of length 2m. Friction during the sliding action of the cylindrical projectile down the guide pipe is considered to be negligible.
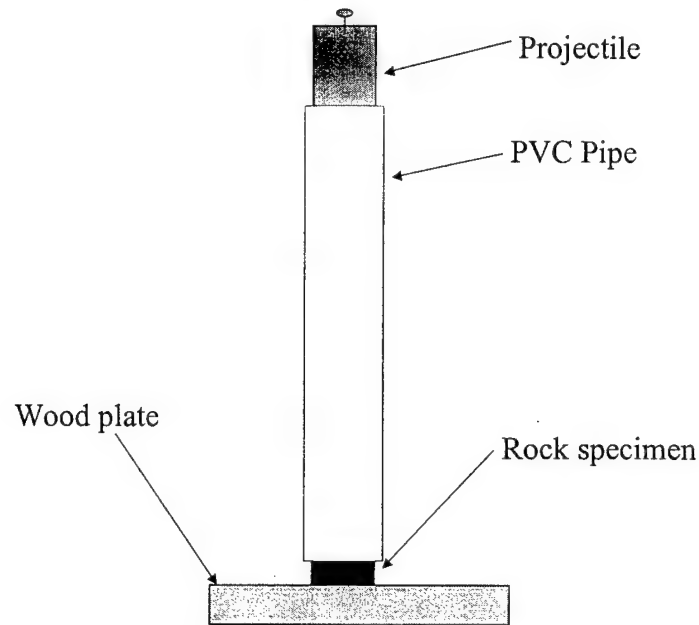
Figure 2. Schematic of Free-Drop System

Since the impactor is released from rest, the kinetic energy at impact (for one drop) is given by $KE = \frac{1}{2}mv^2 = mgh$, where m = impactor mass, h = drop height and g is the acceleration of gravity. For the experimental system, the mass and height were held constant, and therefore the input energy was controlled by the number of drops on each specimen (varying from 1 to 5). It was assumed that each impact generated additional damage within the specimen.

In order to understand the effect of this impact damage, each of the impacted granite specimens were compression tested in a servo-hydraulic, compression testing machine. The testing machine was driven and controlled by a computer, and load and displacement were collected using a data acquisition system at a sampling rate of 0.1

points/second. Specimens were loaded at a constant displacement rate of 0.0001 in/sec up to failure.

Results of the granite compression experiments are shown in Figure 3. Two groups of specimens were tested, each containing specimens with similar levels of induced damage. The stress-strain curves are labeled with the number of impacts each specimen received. The experimental data shows that for the cases of low impact damage, potential microcracks and pre-existing defects affect only the compression strength. For these cases (1 or 2 drops), the rock specimens still behave essentially in an elastic and brittle fashion. However, for the cases of input damage as a result of 3 or more drops, a change-in the stress-strain response is clearly evident. It appears that the initial slope of the stress-strain curves are not greatly affected by input damage; however, the ultimate strength and softening behavior is most definitely a function of the damage due to induced damage.

1: m=100, ε_0=0.019
2: m=76.5, ε_0=0.0148
3: m=67, ε_0=0.0128
4: m=52.5, ε_0=0.00935
5: m=6.6, ε_0=0.0084
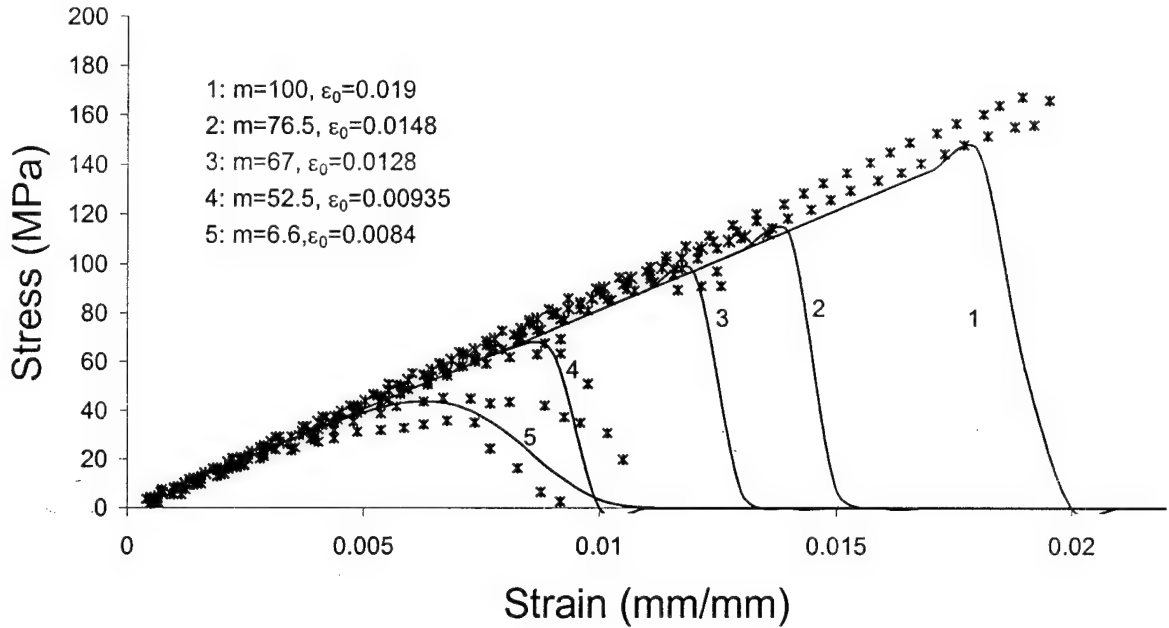
Figure 3. Stress/Strain Plots and Model Results for Granite Compression Testing

Also shown in Figure 3. are the model predictions from relation (8). The theoretical stress-strain curves were generated by appropriate choices of the model parameters, m and ε_o. The theoretical results agree reasonably well with the experimental data. The damage parameter D is the function of the strain applied on the granite specimen, and ε_0, m are related to the initial damage. Therefore, different amounts of input damage will yield different values for the model parameters ε_0 and m. Figure 4 shows the behavior of the m and ε_0 -parameters verses the input energy. It was observed that both m and ε_0 decreased with the amount of input energy. In general, rock damage increases with the applied strain. For initial damage from 1 to 5 drops, the damage growth with strain was found to be somewhat different. There is some indication

8

that the damage parameter undergoes a more sudden change for the lower number of drops. This would mean rock behaves more brittle with less initial damage.
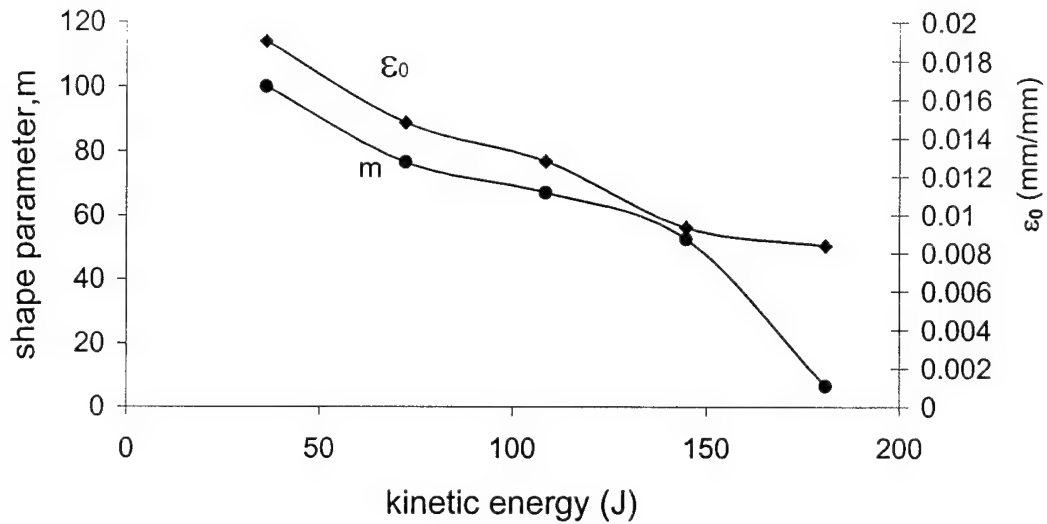
Figure 4. ε_0 and m versus Input Kinetic Energy

Figure 5 shows the experimentally determined relationship between input kinetic energy (producing damage) and the specimen's compression strength. It was observed that the compression strength of the granite specimens decreases with the input energy.
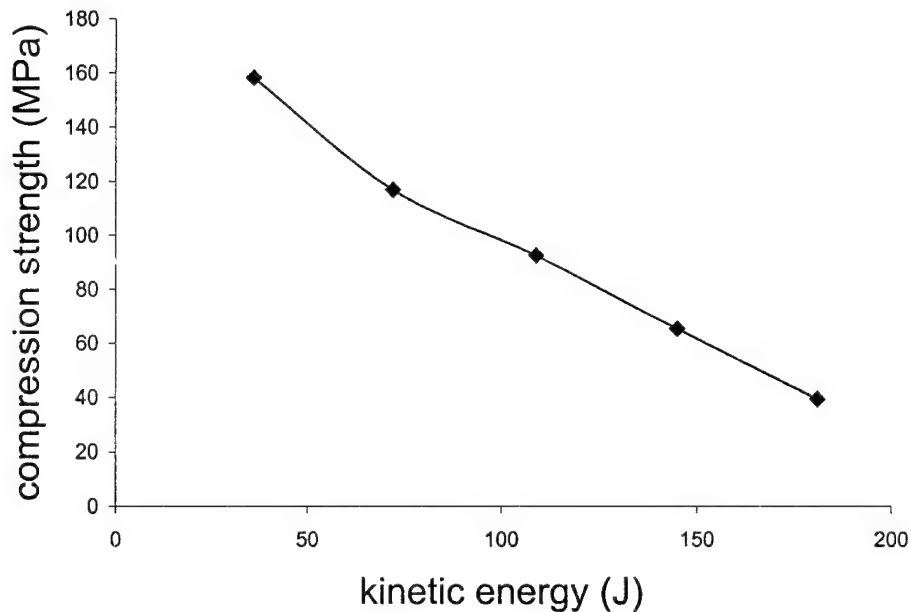
Figure 5. Granite Compression Strength versus Input Kinetic Energy

1.4 COMPRESSION TESTING OF CONCRETE

For comparison to the brittle granite compression testing results, a more 'ductile' concrete was tested in a similar manner. By its nature, concrete is less homogenous than granite due to its aggregate composition, larger internal defect size, and higher defect density. An Air Force, "G" mixture of concrete was used for this testing. Its unconfined compressive strength, 40.5 MPa, is about five times lower than the strength of the Barre granite.

The testing was conducted using the method described in ASTM C39, Compressive Strength of Cylindrical Concrete Specimens [27]. The specimens were cast in two inch diameter cylinders, and faced off at four inch lengths to achieve parallel ends.

Damage was induced in the concrete in a similar manner to the granite, however a weight of 807 gm, dropped from a height of 60 inches was used due to the lower strength of the concrete. The number of weight drops was increased until visible damage was

10

evident in the specimens. Early testing of specimens impacted by the weight showed no decrease in compressive strength until visible damage was evident. Due to the non-homogeneity of concrete, it was difficult to control the amount of damage. Some specimens would appear intact after twenty (20) impacts whiles others were completely destroyed after only ten (10).

Upon failure, each specimen displayed a similar lateral splitting mechanism, regardless of the amount of damage induced. Similar to the granite testing, the concrete exhibited a decrease in compressive strength with increased levels of induced damage. However, the concrete displayed a less severe drop in load carrying capability on the downward sloping side of the stress/strain curve. The greater the slope of this portion of the stress/strain curve the more brittle the material. Therefore, while both materials displayed a decrease in brittleness with increasing damage, the concrete is less brittle than the granite in an undamaged state. Figure 6 shows a group of stress/strain curves for concrete specimens with different degrees of damage. Figure 7 is a plot of maximum compressive strength versus input damage energy. As shown the strength decreases non-linearly with damage.
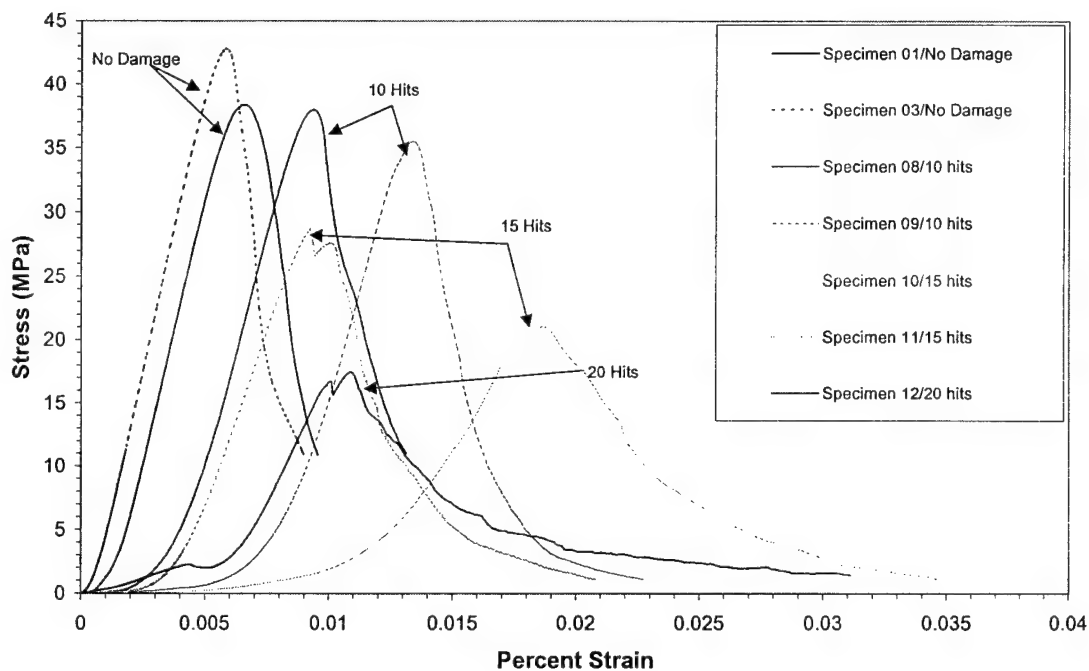
Figure 6. Concrete Static Concrete Strength versus Strain
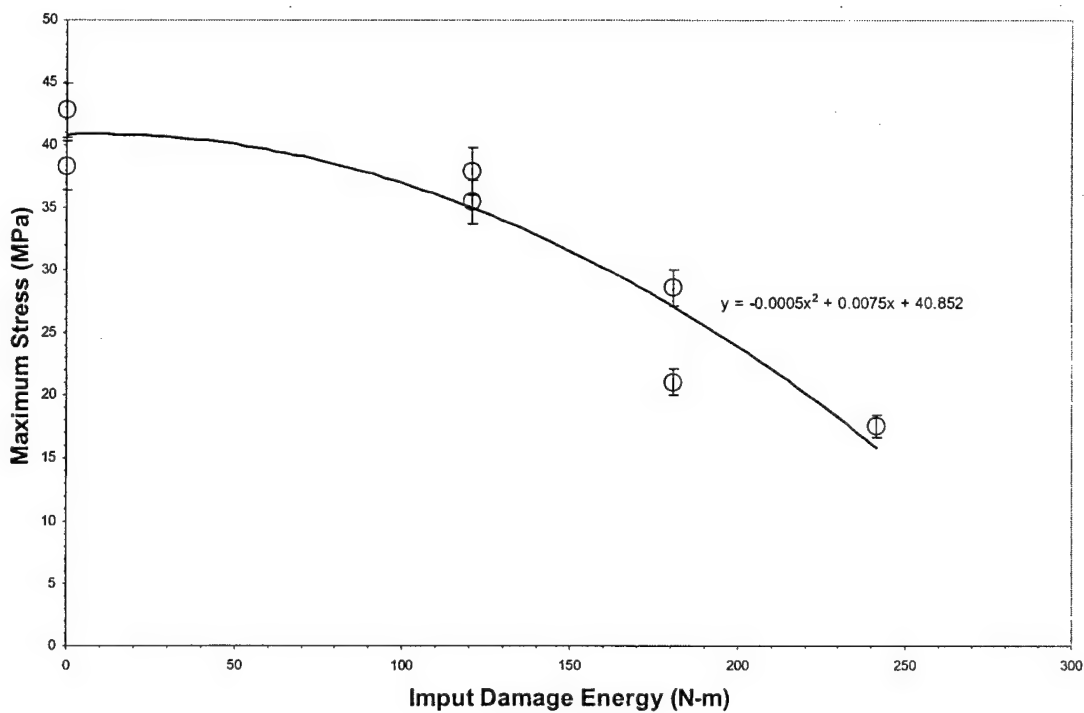
Figure 7. Maximum Concrete Strength versus Input Damage Energy

12

Another effect evident is the decreasing slope of the linear, loading portion of the stress curve with increasing damage. This effect was not evident in the granite testing, where the slope of this portion of the curve remained approximately constant with damage. In the granite model equation (8), E remains constant with damage, and this appears to be adequate for the granite, but not for concrete. An empirically determined scaling factor was developed which takes into account the variation of E with damage and is given by

$$E' = 0.2E_{max}\,e^{0.2m} \tag{9}$$

and this is incorporated into the stress/strain law

$$\sigma = E'\varepsilon\,e^{-\left(\frac{\varepsilon}{\varepsilon_0}\right)^m} \tag{10}$$

where E' is the slope of the stress/strain curve with induced damage, and E_{max} is the slope of the undamaged stress/strain curve. Figure 8 shows that by properly choosing m and ε_0, the model can predict the stress/strain curve of damaged concrete with a reasonable degree of accuracy. Currently, efforts are under way to find a physical meaning for the values of the model parameters.
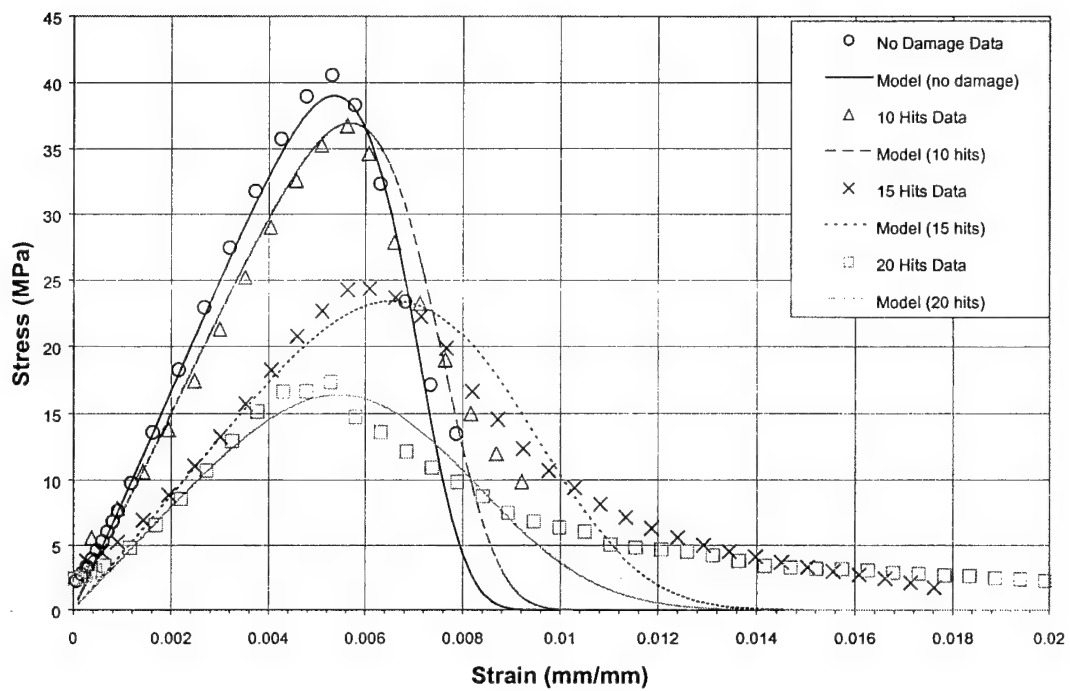
Figure 9. Modified Static Model for Concrete Strength versus Strain.

1.5 DYNAMIC COMPRESSION STRENGTH OF GRANITE AND CONCRETE

Rock or concrete subject to high-speed impact loading normally fail within 10^{-4} to 10^{-2} seconds. In such a dynamic loading condition, properties of rock or concrete, such as strength and damage character, will be considerably different from those in a static condition. Therefore, it is important for the research to understand fracture properties of rock and concrete under high-speed impact loading.

The objective of this test series is to study the effect of induced damage on the dynamic strength of concrete and rock. It has been shown that the dynamic strength of rock like materials increases with strain rate, up to levels almost double the static strength [10]. Due to this, it was hypothesized that by inducing damage, which is essentially increasing the density of the pre-existing flaws in the material, the dynamic strength would decrease as in the static case. However, the opposite result was actually observed during the testing. This effort is still in process so no results are reported here.

1.6 REFERENCES:

[1] Forrestal, M. J, (1986), "Penetration into Dry Porous Rock", Int'l J. of Sol. And Struct. ,22, pp.1485- 1500.

[2] Forrestal, M. J. and Luk, V. K., (1992), "Penetration into Soil Targets", Int'l J. of Impact Engng, 12, pp. 427-444.

[3] Forrestal, M. J. et al, (1994), "An empirical Equation for Penetration Depth of Ogive Nose Projectiles into Concrete Targets", Int'l J. of Impact Engng., 15, pp.395-405.

[4] Canfield, J. A. and Clator, I. G., (1966), " Development of A Scaling Law and Techniques to Investigate Penetration in Concrete", NWL Report No. 2057.

[5]   Heuze, F. E., (1990), "An overview of Projectile Penetration into Geological Materials, with Emphasis on Rocks", Int. J. Rock Mech. Min. Sci. & Geomech. Abstr., 27(1), pp.1-14.

[6]   Pang, S. S., Goldsmith, W., and Hood, M.,(1989), "A Force-Indentation Model for Brittle Rocks", Rock Mechanics and Rock Engineering, 22, pp.128-148.

[7]   Lundberg, B., (1974), " Penetration of Rock by conical Indenters", Int. J. Rock Mech. Min. Sci. & Geomech. Abstr., 11, pp. 209-214.

[8]   Kou Shao-Quan, Lindqvist, P-A and Tan, Xiang-chun (1995), "An Analytical and Experimental Investigation of Rock Indentation Fracture", the 8th International Congress on Rock Mechanics, Japan, F1-F4.

[9]   Li, G., Shukla, A. and Sadd, M., "The Effect of Damage on the Uniaxial Compression Behavior of Granite", (1998), Submitted to Journal of Engineering Mechanics.

[10]   Blanton, T. L., (1981), " Effect of Strain Rates from 10^{-2} to 10 1/sec. In Triaxial Compression Tests on Three Rocks", Int. J. Rock Mech. Min. Sci. & Geomech. Abstr., 18, pp.47-62.

[11]   Weibull, W. (1939) "A Statistical Theory of The Strength Of Materials", Royal Swedish Academy of Eng. Sci. Proc. No.151, 1-45.

[12]   Hudson, J. A. and Fairhust, C., (1969) "Tensile strength, Weibull's theory and a general statistical approach to rock failure", The proceedings of the Southampton 1969 civil engineering materials conference (part II), Edited by M. Te'eni. 901-914.

[13]   Krajcinovic, D. and Silva, M. A. G., (1982) "Statistical Aspects of the Continuous Damage Theory", Int. J. Solids Structures, 18(7), 551-562.

[14]   Weber, P. and Saint-Lot, (1983), "A Statistical Model of Macroscopic Failure Under Compression", 5th International congress on Rock Mechanics, Edited by A.A. Balkema, Rotteroam, A161-164

[15]   Wiederhorn, S. M., (1981), "A Probabilistic Framework For Structural Design", Fracture Mechanics of Ceramics, R. C. Bradt, D.P.H. Hasselman & F.F. Lange, (Eds.), Plenum Press, New York, V, 197-226.

[16]   Tang, C.A., (1988), "Experimental Study Of Rock Failure", Ph. D thesis, Northeastern University, Shenyang, China.

[17]   Jaeger, J.C. & Cook, N.G.W., (1979), Fundamentals of Rock Mechanics, 3rd Edn., Fletcher & Son Ltd, Norwich, Great Britain.

[18]   Swan, G., (1980a), "Fracture Stress Scale Effects For Rocks In Bending", Int. J. Rock Mech. Min. Sci.& Geomec. Abstr., 17, 317-324.

[19] Ratigan, J. L., (1981), "A Statistical Fracture Mechanics Approach to the Strength of Brittle Rock", Ph.D. Thesis, Univ. of California, Berkeley, California.

[20] Medrano, R.E. & Grills, P.P., (1987), "Weibull Statistics: Tensile And Bending Tests", J. Am. Ceram. Soc., 70. No.10, C230-C232.

[21] Priest, S.D. & Hudson, J.A., (1976), "Discontinuity Spacing in Rock", Int. J. Rock Mech. Min. Sci. & Geomech. Abstr., 16, 33-362.

[22] Priest, S.D. & Hudson, J.A., (1981), "Estimation Of Discontinuity Spacing And Trace Length Using Scanline Curves", Int. J. Rock Mech. Min. Sci. & Geomech. Abstr., 18, 183-187.

[23] Sen, Z. and Kazi, A., (1984a), "Discontinuity Spacing And RQD Estimates From Finite Length Scanlines", Int. J. Rock Mech. Min. Sci. & Geomech. Abstr., 21, 203-212.

[24] Sen, Z., (1984b), "RQD Models and Fracture Spacing", J. Geotech. Engng ASCE 110, 203-216.

[25] Rouleau, A. and Gale, J. E., (1985), "Statistical Characterization Of The Fracture System In The Stripa Granite", Sweden, Int. J. Rock Mech. Min. Sci. & Geomech. Abstr.,22, 353-367.

[26] Bardsley, W.E. , Major, T. J. and Selby, M. J., (1990), "Note On A Weibull Property For Joint Spacing Analysis", Int. Jour. of Rock Mech. Min. Sci. & Geomech. Abstr. 27, 133-134.

[27] ASTM C39, "Compressive Strength of Cylindrical Concrete Specimens"

[28] Dutta, P. K., (1971), "A Theory of Percussive Drill Bit Penetration", Int. J. Rock Mech. Min. Sci., 9, pp.543-567.

CHAPTER 2   PHOTOELASTIC EVALUATION OF STRESS FIELDS AND FRACTURE DURING DYNAMIC SPLITTING EXPERIMENTS

2.1 ABSTRACT

Dynamic tensile-splitting experiments were conducted on brittle polyester discs, Homalite-100, to photoelastically visualize stress field development in the specimens and, ultimately, specimen fracture. A Split Hopkinson Pressure Bar (SHPB) was used to dynamically load the specimen and record load data as a function of time. Images of the stress field were captured with high-speed photography and interpreted using photoelastic analysis. The experiments determined that the specimens reached an equilibrium state relatively quickly, and remained in equilibrium until fracture. Fracture began with in plane cracks on either side of the specimen and from these emanated transverse cracks, which propagated across its mid-plane at velocities up to 60% of the shear wave velocity in the material. Contact loads calculated from photoelasticity agreed favorably with SHPB results. These experiments also allowed for the determination of the dynamic splitting strength of the Homalite-100 as a function of strain rate. The dynamic splitting strength of the material increased with the increasing strain rate, reaching a maximum value of about twice the static splitting strength.

2.2 INTRODUCTION

Tensile splitting experiments offer a convenient method to determine the tensile strength of brittle materials, such as concrete and rock. The method utilizes a cylindrical sample and compressive testing machine similar to those used to perform compression

strength experiments. Recently, researchers have been investigating the effect of strain rate on the tensile strength of concrete materials. It had been established that the compressive strength of concrete and rock materials increases up to approximately two times the static strength at high strain rates [1], whereas, the tensile strength has been shown to increase up to seven times the static strength at similar strain rates. [2]. To perform these high strain rate experiments in both compression and tension, a Split Hopkinson Pressure Bar (SHPB) apparatus is used to apply the dynamic loading and to calculate the specimen response.

To ensure that this methodology is valid for the determination of dynamic tensile splitting strength, a photoelastic experiment was designed to observe stress field development during dynamic loading, to check if the loads calculated from the SHPB strain gages are accurate, and to determine whether the specimen under study was subjected to uniform loading, i.e. was in equilibrium, at the time of fracture. If these conditions are indeed met, dynamic splitting strength can be derived from the relationships used to calculate static splitting strength. Also, by varying the pressure used to propel the projectile into the SHPB incident bar, the strain rate can be varied to determine its effect on the Homalite-100 splitting strength.

The dynamic tensile splitting experiments were performed on a 12.7 mm SHPB using Homalite-100 discs as the specimens. The 25.4 mm diameter, transparent discs were held diametrically between the SHPB incident and transmission bars. A 203 mm long projectile was fired from a gas gun at a pressure level sufficient to create a compressive wave in the incident bar that would cause tensile splitting failure in the specimens. Photoelastic fringe patterns of the stress field were created by projecting

19

polarized light through the specimen, and captured using an Imacon 468 high-speed digital camera, manufactured by Hadland Photonics. The high-speed digital camera was also used to record crack propagation and failure in the specimens.

From the experiments, it was shown that the specimens reached a state of equilibrium within 30 microseconds from the initial arrival of the compressive wave. The equilibrium condition, i.e. equal loads at each specimen contact point, was confirmed in both the strain data recorded by the SHPB and the fringe patterns captured by the camera. In all cases, the specimen was in equilibrium for a relatively long time, approximately 60 microseconds, prior to crack initiation. This result is important for the determination of the dynamic splitting strength using the maximum load recorded in the SHPB transmission bar. With the specimen in equilibrium prior to failure, the maximum load transmitted by the specimen into the transmission bar is the maximum load the entire specimen is subjected to during the experiment. Assuming the stress field is quasi-static, the dynamic splitting strength may be calculated using this maximum, or failure, load and the static relationship. For this study, the dynamic splitting strength of Homalite-100 was shown to increase to approximately 1.9 times the static splitting strength. Currently the loads at each contact face are being calculated using the strain gage data as well as the photoelastic fringe patterns to ensure that they agree.

The photographs also recorded the crack propagation and failure of the specimens. These pictures showed that the cracks propagated at velocities up to 750 m/s, or 60% of the shear wave velocity, along the loading line of the specimens. The failure pattern of the specimens was consistent with both static and dynamic tensile splitting

tests recently performed on concrete and rock specimens at the University of Rhode Island [3].

2.3 EXPERIMENTAL PROCEDURE

2.3.1 *Quasi-Static Tensile Splitting Experiments*

ASTM standard Brazilian, or Tensile Splitting Experiments, are usually performed on concrete or rock specimens (C496 and D3967 respectively) [4, 5]. For these types of materials it is difficult to fabricate and test typical "dog bone" specimens. The Brazilian tensile test was developed in order to indirectly determine the tensile strength of brittle materials using cylindrical specimens. Based on elasticity theory, the two-dimensional stress field in the disc can be derived and then simplified to examine only the stress along the loading line [6]. Taking into account the specimen thickness, L, the stress distribution for the Brazilian splitting test is given by Equation 1, with parameters defined in Figure 1. [7]

$$\sigma_y = \frac{2P}{\pi L D}\left[\frac{D^2}{r(D-r)}-1\right] \qquad (1a)$$

$$\sigma_x = \frac{2P}{\pi L D} \qquad (1b)$$
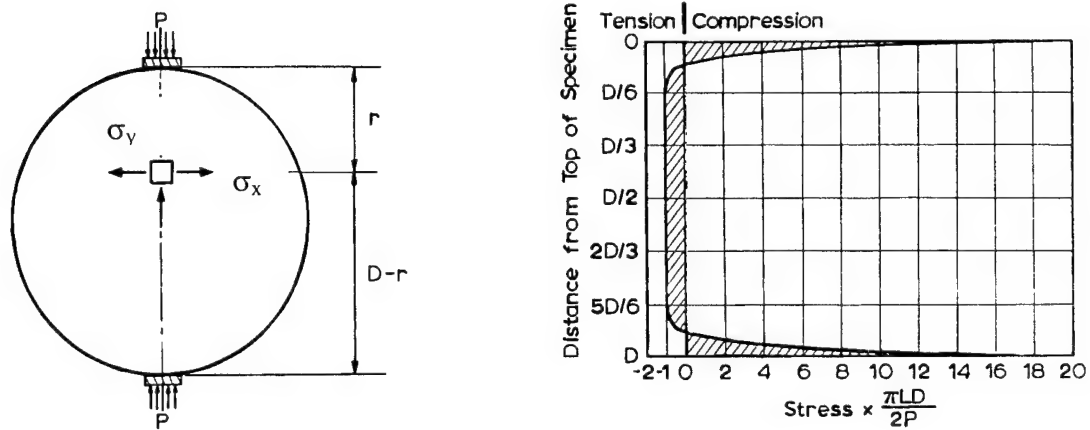
Figure 1. Brazilian Test Schematic and σ_X Stress Distribution Along Loading Line. [7]

As shown, a constant tensile stress, σ_x, is generated along the loading line. At the loading points the elasticity solution is no longer valid due to the singularity of the loading. At these points there exists a bi-axial state of compressive stress of equivalent levels, which along with the bearing blocks used to apply the load, allow the specimen to fail in tension along the loading line and not locally by compression. As expected, Homalite-100, being a brittle material with a relatively low tensile strength compared to its compressive strength, will tend to fail in tension along the loading line. For each of the splitting tensile experiments the maximum load, P, was used to calculate the splitting stress, σ_x, at failure using Equation 1b.

For the static experiments, 25.4 mm diameter, 6.4 mm thick, Homalite-100 discs were loaded diametrically in a screw driven Instron Testing machine. The specimens were loaded in steps by the Instron at a carriage rate of 0.127 mm/sec. To record the load at failure, the load cell output was connected to a storage oscilloscope. The failure load was then used to calculate the tensile splitting strength by Equation 1b.

22

2.3.2 *Dynamic Tensile Splitting Using a Split Hopkinson Pressure Bar*

In order to perform tensile splitting experiments under dynamic loading, a Split Hopkinson Pressure Bar (SHPB) was used in compression. However, instead of sandwiching the specimen lengthwise between the bars, the specimen was held diametrically between the bars using steel bearing bars to avoid localized failure due to the point load. Figure 2 shows the dynamic splitting test setup.
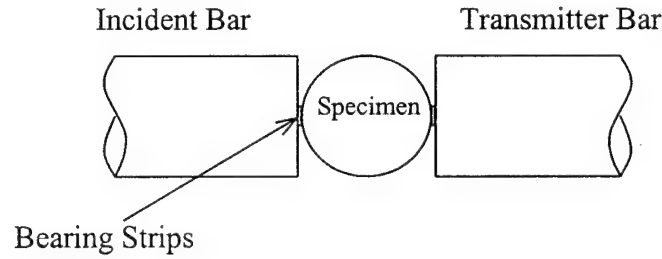
To load the specimen, the incident bar is impacted with a projectile fired from a gas gun, which creates a compressive wave traveling down the bar. At the specimen, this wave will be partially reflected back into the incident bar and partially transmitted into the transmitter bar. Strain gages mounted at the mid points of both bars are used to record the strain waves. Assuming one-dimensional wave propagation, and negligible attenuation of the waves, or strain pulses, in the steel bars, the loads on each end of the specimen can be calculated as a function of time by [10]

$$P_1 = A_b E_b \left(\varepsilon_i + \varepsilon_r \right) \tag{2a}$$

$$P_2 = A_b E_b \varepsilon_t \tag{2b}$$

where P_1 and P_2 are the loads on the incident and transmitted bar contact faces respectively, A_b is the bar cross sectional area, E_b is the bar material Young's modulus, and ε_i, ε_r, ε_t are the incident, reflected, and transmitted strain pulses shifted in time to account for the mid bar location of the strain gages.

For specimens in compression the SHPB analysis assumes that the load on each specimen face is equal, so that the specimen is in equilibrium. With this assumption the specimen stress/strain response can be calculated [10]. However, for the dynamic splitting experiment the standard analysis to obtain the specimen stress can no longer be used. For these experiments it has been assumed that the peak tensile splitting stress of the cylinder is proportional to the peak transmitted compressive strain measured in the transmitter bar by Equation 1b [2], and that the load P is now defined by Equation 3, where R_{bar} and E_{bar} are the transmitter bar radius and Young's modulus respectively, and ε_t is the strain measured in the transmitter bar.

$$P = \pi R_{bar}^2 E_{bar} \varepsilon_t \qquad (3)$$

Determining the validity of using the static relations for dynamically loaded specimens is a main objective of this experimental study. For the static relation to be valid, the specimen must be in equilibrium. In similar experiments involving dynamic wave propagation in a chain of discs, it was shown that if the loading pulse width is much longer than the disc diameter, quasi-static stress field equations were valid in a region close to the contact point [11]. For the SHPB dynamic loading in this study, the incident

pulse length is related to the projectile length. Therefore, all the experiments were performed on a 12.7 mm SHPB setup using a 203 mm long projectile, giving a strain pulse of approximately 406 mm in length. The gas gun pressure was initially varied from 0.207 MPa to 0.414 MPa to determine the pressure required to obtain fracture in the specimen. The specimens for all the dynamic splitting experiments were Homalite-100 discs, 25.4 mm in diameter and 6.4 mm thick.

2.3.3 *High Speed Photoelasticity and Fractography*

To capture the stress field, and the photoelastic fringes in the specimens during the dynamic splitting experiments, an Imacon 468 high-speed digital camera was used. The camera, manufactured by Hadland Photonics, is capable of taking seven pictures at a framing rate of up to 200 million/second, with exposures as short as 5 nanoseconds. In this set-up, the camera was set to trigger off the incident strain pulse, send a flash command to a light unit, and begin taking a timed sequence of pictures at a given time from the initial signal. All the images were taken with an exposure time of 300ns unless otherwise stated. The versatility of the image timing allowed a series of photographs to be taken from a single experiment, capturing different events. A schematic of the experimental set-up is shown in Figure 3.
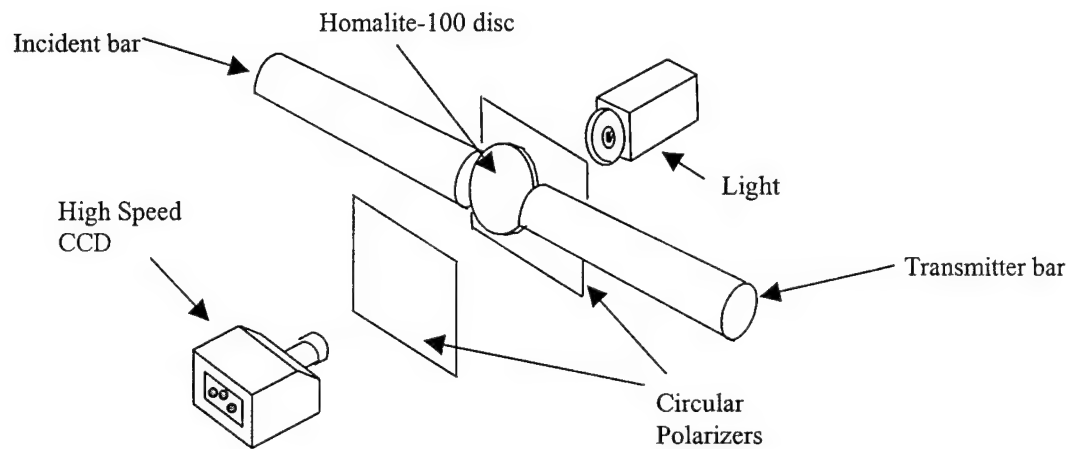
Figure 3. Schematic of Photoelastic Study of Dynamic Splitting Stress Field.

The camera's imaging software is also capable of being calibrated from a known distance (disc diameter) on an image in order to record position measurements. This allowed the true crack location to be determined as a function of time during the fracture process. The image analysis software of the camera was then utilized to determine the crack velocity and acceleration. These results will be presented in the following sections.

2.4 THEORETICAL CONSIDERATIONS

2.4.1 Contact Load Determination from Photoelasticity

From the images recorded using the high-speed digital camera, the dynamic stress field during the SHPB experiments was observed, and the contact loads on the specimens were calculated using the photoelastic fringe patterns. Homalite-100, whose properties are listed in Table 1, is a transparent polymer ideally suited for photoelastic studies.

Table 1. Homalite-100 Properties.

Dynamic Young's Modulus, E (GPa)	5.3
Poisson's Ratio, ν	0.35
Density, ρ (kg/m^3)	1230
Optical Fringe Constant, f_σ (kN/m)	23.7
P wave Velocity, C1 (m/s)	2220
S wave Velocity, C2 (m/s)	1270
Rayleigh Wave Velocity, CR (m/s)	1186

These properties allow the use of polarized light to visualize isochromatic "fringes" in the material under load. Isochromatic fringes, which are contours of constant maximum shear stress, can be used to determine the stress field through the stress optics law, which states:

$$\tau_{max} = \frac{\sigma_1 - \sigma_2}{2} = \frac{N_f f_\sigma}{2h} \tag{4}$$

where σ_1 and σ_2 are the in-plane principal stresses, N_f is the fringe order, f_σ is the optical constant of the material and h is the specimen thickness. A photoelastic method to calculate the load between two discs in contact was developed by Shukla and Nigan [8], where the disc contact geometry is defined in Figure 4.
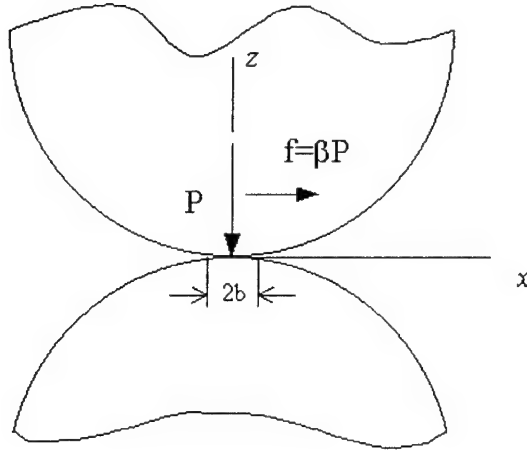
Figure 4. Geometry of Disc Contact [8].

The stress field around the contact region is then given by

$$\sigma_{zz} = -\frac{b}{\pi\Delta}\left\{z\left(b\phi_1 - x\phi_2\right) + \beta z^2\phi_2\right\} \tag{5a}$$

$$\sigma_{xx} = -\frac{b}{\pi\Delta}\left[z\left(\frac{b^2 + 2z^2 + 2x^2}{b}\phi_1 - \frac{2\pi}{b} - 3x\phi + \beta z^2\phi\right) + \beta\left\{\left(2x^2 - 2b^2 - 3z^2\right)\phi_2 + \frac{2\pi x}{b} + 2\left(b^2 - x^2 - z^2\right)\frac{x}{b}\phi_1\right\}\right] \tag{5b}$$

$$\sigma_{zx} = -\frac{b}{\pi\Delta}\left[z^2\phi_2 + \beta\left\{\left(b^2 + 2x^2 + 2z^2\right)\frac{z}{b}\phi_1 - 2\pi\frac{z}{b} - 3xz\phi_2\right\}\right] \tag{5c}$$

where ϕ_1 and ϕ_2 are defined as

$$\phi_1 = \frac{\pi(M + N)}{MN\sqrt{2MN + 2x^2 + 2z^2 - 2b^2}} \tag{5d}$$

28

$$\phi_2 = \frac{\pi(M-N)}{MN\sqrt{2MN+2x^2+2z^2-2b^2}} \tag{5e}$$

$$M = \sqrt{(b+x)^2 + z^2} \quad \text{and} \quad N = \sqrt{(b-x)^2 + z^2} \tag{5f}$$

and Δ is defined as

$$\Delta = \frac{1}{A}\left(\frac{1-v_1^2}{E_1} + \frac{1-v_2^2}{E_2}\right) \; ; \; A = \frac{1}{2}\left(\frac{1}{R_1} + \frac{1}{R_2}\right) \tag{5g}$$

where v, E, and R are the Poisson's ratios, Young's moduli, and radii of the two discs in contact. Using a Newton-Raphson, multi-point iteration method, the unknown contact width, b, and friction factor, β, can be calculated using equations 2 and 3 for any large number of (x, z) points taken along fringes of order N_f near the contact region [8, 9]. Then the contact load P on the disks can be calculated by

$$P = \frac{\pi b^2 h}{2\Delta} \tag{6}$$

In the present SHPB experiments, the disc is being contacted by a flat plane so R_2 can be taken as infinity, simplifying the expression for A.

Since fringe pattern photographs of the Homalite-100 discs were taken at the static loads steps applied in the Instron machine, the loads calculated using the method described could be compared to the measured load data from the Instron load cell.

2.5 RESULTS AND DISCUSSION

For this experimental study a total of twenty-three (23) tensile splitting experiments were performed on 25.4 mm diameter Homalite-100 discs; two (2) static and twenty-one (21) dynamic. The static experiments provided a baseline static splitting strength of Homalite-100, and static fringe pattern photographs of the splitting stress field. Since the fringe patterns photographs, taken at known static loads, provided good calibration data for the photoelastic method used to calculate the contact loads on the discs.

The twenty-one (21) dynamic experiments provided the stress field visualization and SHPB data required to determine the equilibrium state of the specimen. They were also used to observe crack propagation and specimen failure. The first seven (7) dynamic experiments were performed at low-level loading, i.e. low SHPB gun pressure, to investigate the development of the stress field. The last fourteen (14) experiments were performed at load levels sufficient to cause specimen fracture. These experiments were performed to investigate the Homalite-100 dynamic splitting strength as a function of strain rate, and to observe fracture and crack propagation in the specimens.

2.5.1 Static Tensile-Splitting Results

2.5.1.1 Static Tensile-Splitting Strength of Homalite-100

The static tensile splitting strength of the Homalite-100 material was calculated with equation 1b using the disc geometry and the baseline static load data from the two (2) Instron experiments. The results of the two (2) experiments yielded the static splitting

strengths were 27.34 MPa and 30.72 MPa for an average Static Splitting Strength of
29.03 MPa for the Homalite-100 material.

2.5.1.2   Photoelastic Visualization of Static Splitting Stress Fields

Figure 5 shows the static fringe patterns for a Homalite-100 specimen subjected to
a splitting load. As shown, the fringe patterns emanate from the contact points. As the
load is increased, the fringe density increases and ultimately a splitting fracture will
occur.
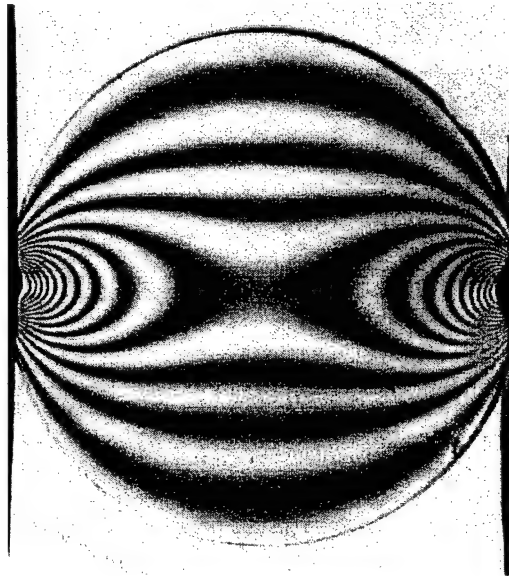
Figure 5. Static Splitting Fringe Pattern for Homalite-100 Specimen

The fringe patterns for the static experiments were taken using a Nikon Coolpics 950
digital camera with a monochromatic filter.

2.5.2 Dynamic Tensile-Splitting Results

2.5.2.1   Development of Stress Field

In a dynamic splitting tensile experiment a typical developing stress field is shown in Figure 6. At time zero the compressive wave is just reaching the incident end of the specimen, and the transmitted end is under no load. After 10 microseconds the wave front has traveled across the specimen and incipient loading has occurred at the transmitter bar contact point. As the compressive stress pulse in the bars continues to load the specimen, the two contact point fringe patterns begin to interact and form a saddle structure similar to that observed in the fringes of the static experiments. After 30 microseconds the specimens are in equilibrium with approximately the same number of fringes emanating from each contact. Except for the magnitude of the load, the 30-microsecond dynamic fringe pattern in Figure 6 is identical to the static fringe patterns in Figure 5.
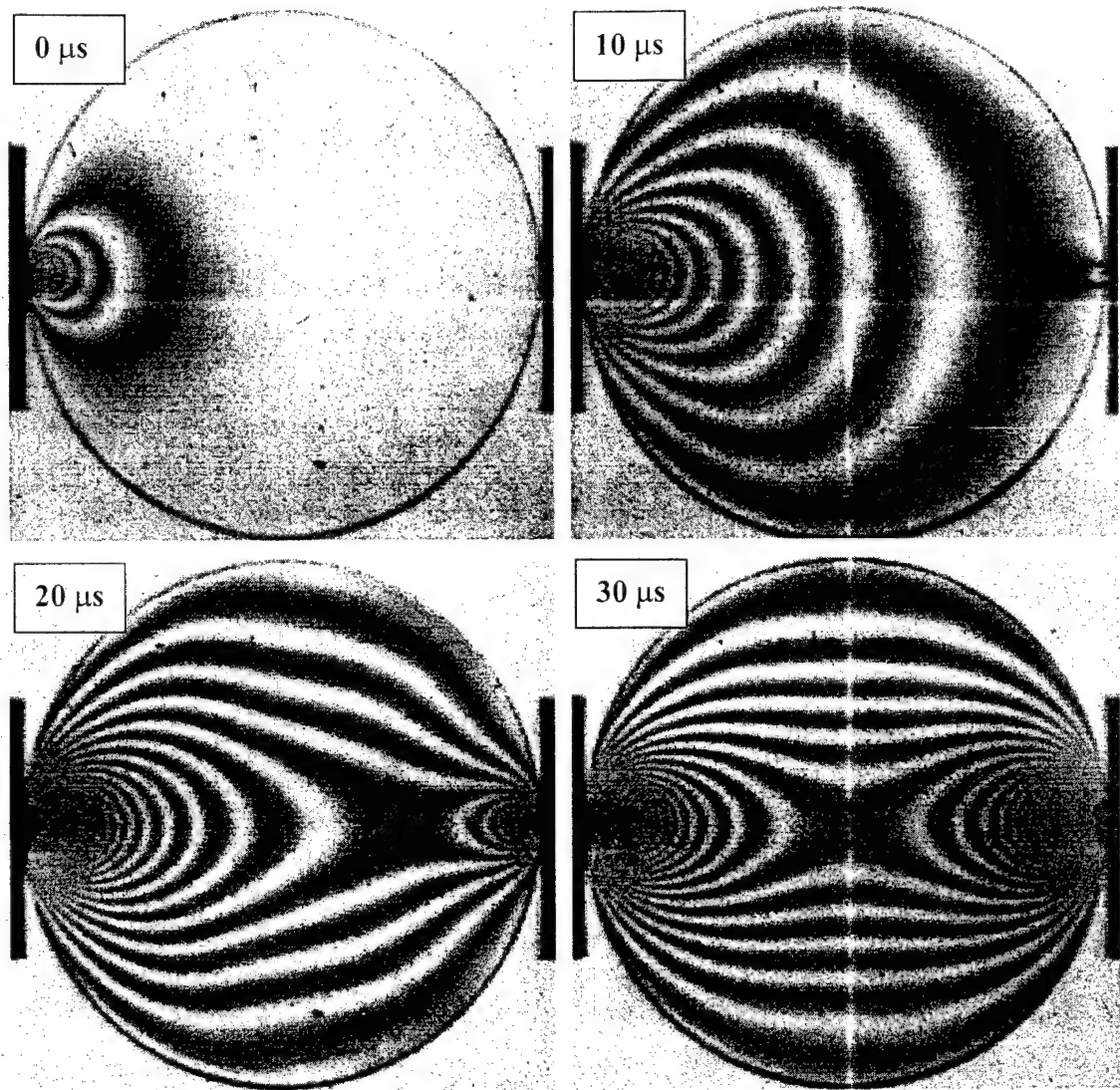
Figure 6. Photoelastic Fringes of Early Stress Field Development in Homalite-100 Disc Subjected to Dynamic Splitting Load (specimen HDS04)

The specimens remain in equilibrium, with the stress pulse reflecting back and forth, increasing in magnitude. The reflections of the stress pulse can be tracked as side-to-side motion of the saddle points seen in the photographs shown in Figure 7. Increase in magnitude of the stress pulse is indicated by an increase in fringe density.
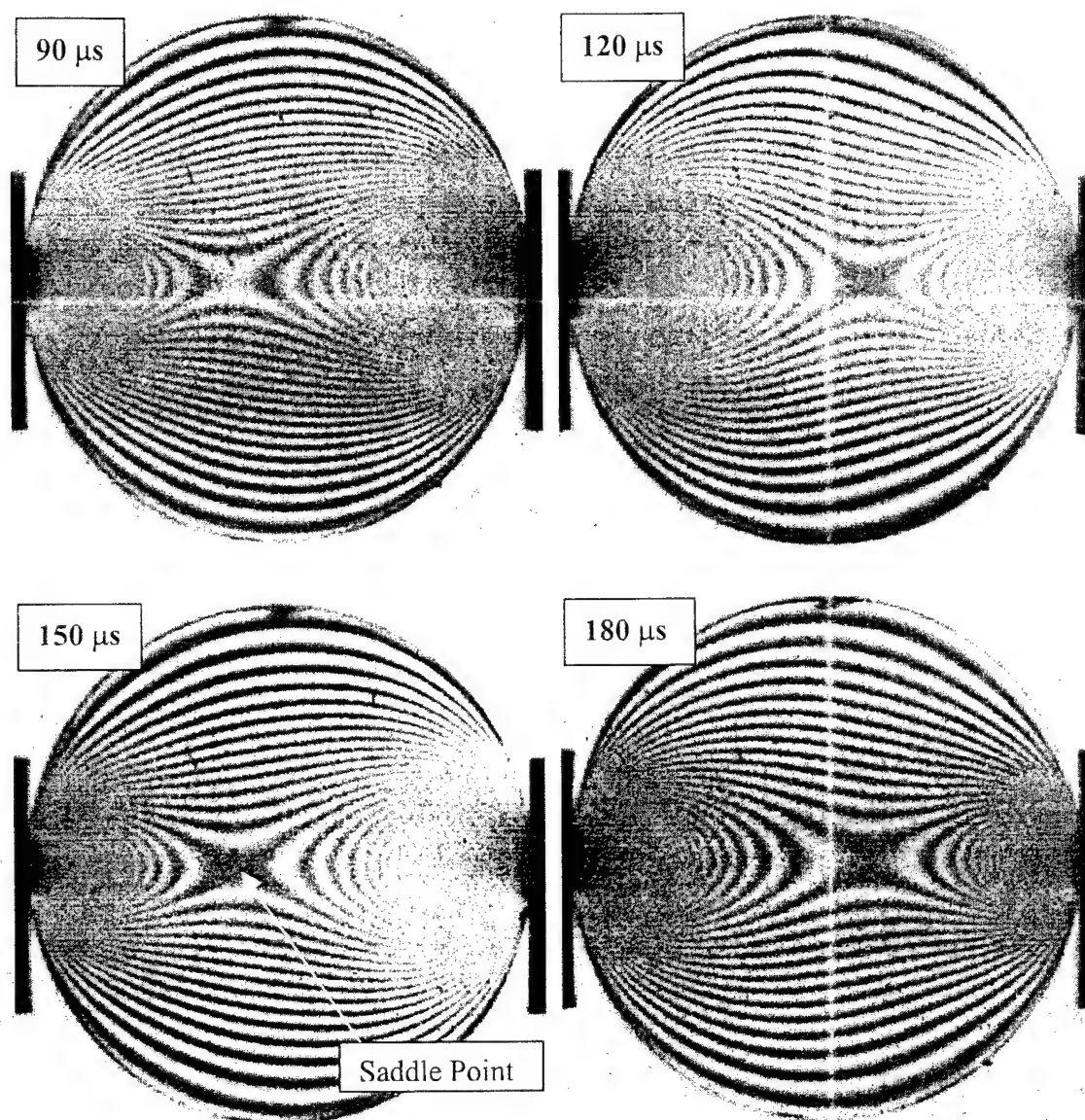
Figure 7. Photoelastic Fringes of Stress Field Movement in Homalite-100 Disc Subjected to Dynamic Splitting Load (specimen HDS07)

Figure 8 is a plot of the saddle point position as a function of time as it oscillates back and forth in the center region of the specimen. As shown, the saddle point moves over a relatively small region of approximately $\pm$ 25% of the disc radius about the center of the specimen.
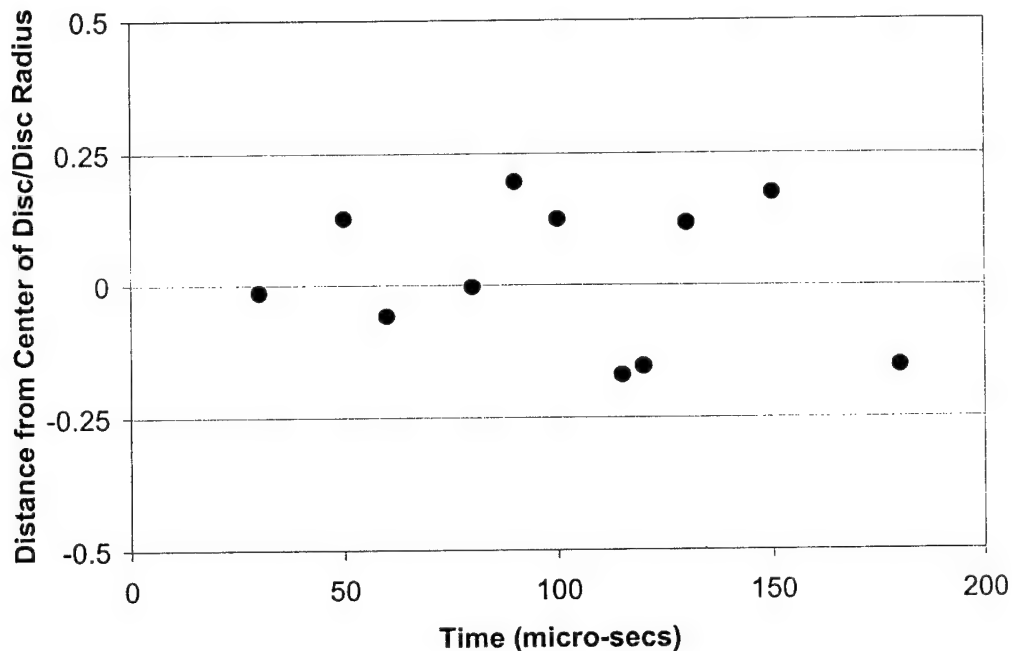
Figure 8. Saddle Point Position as a Function of Time in Dynamic Splitting Specimens

From these results it is evident that although the initial development of the dynamic stress field during a splitting experiment is different than that of the static splitting stress field, the specimen reaches equilibrium in approximately 30 microseconds. Once at equilibrium, the dynamic stress field in the specimen oscillates with relatively small amplitude. This dynamic, but steady state stress field is similar in distribution to that of the static field. Therefore, the use of the static relations to analyze a specimen subjected to dynamic splitting loads appears valid as long as the stress field has adequate time to fully develop.

2.5.2.2   Contact Load Determination

An alternative way to show equilibrium is to calculate the load on the contact faces of the incident and transmission bars using the SHPB strain gage data. Figure 9

35

shows the typical strain versus time data recorded in both incident and transmission bars of the SHPB during a dynamic splitting experiment.
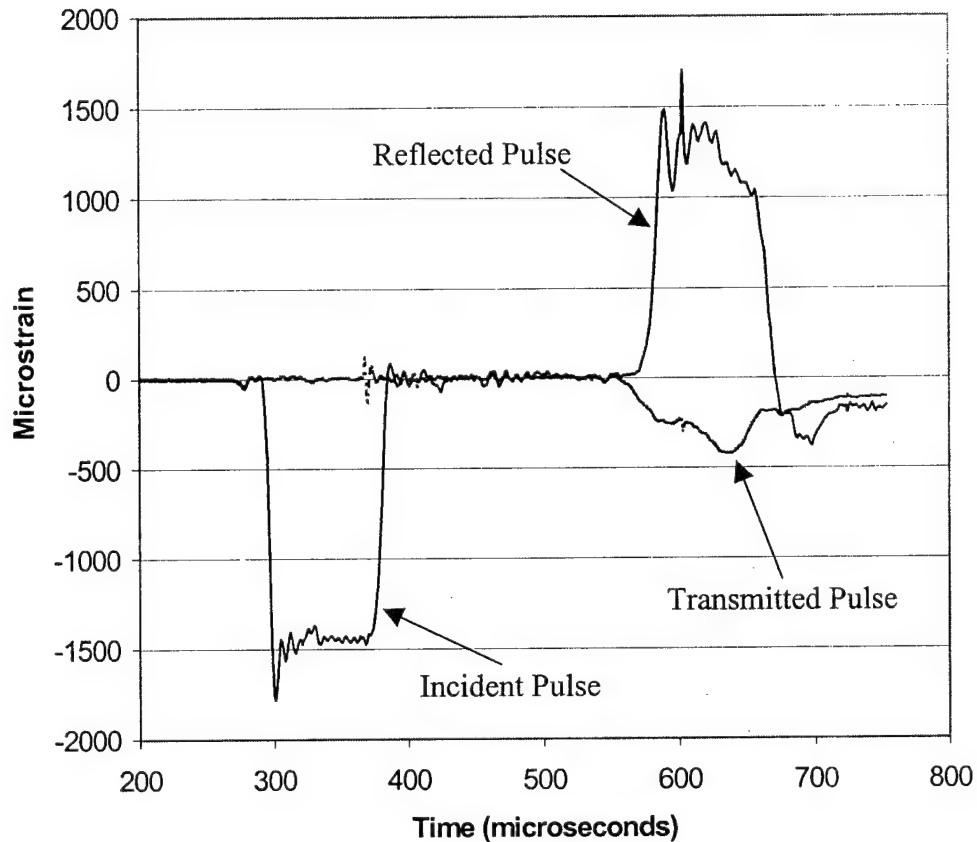
Figure 9. SHPB Strain Gage Data for Dynamic Splitting Experiment on Homalite-100 Specimen (HDS13)

Using this data in Equations 2, the loads on the contact face of each bar can be calculated. This condition for equilibrium requires that the contact loads be equal. Figure 10 is a plot of the contact face loads as a function of time. As shown, the load on the incident face increases as the wave begins to load the specimen, and the load on the transmitter bar face is zero. As the wave travels across the specimen, the load on the transmitter face starts to increase as the incident face load decreases. The loads on each

face become equal at approximately 25 microseconds, and remain equal up to the time of fracture at about 90 microseconds. The time for the equilibrium condition to develop, 25 – 30 microseconds, agrees well with the photoelastic results shown in Figure 6.
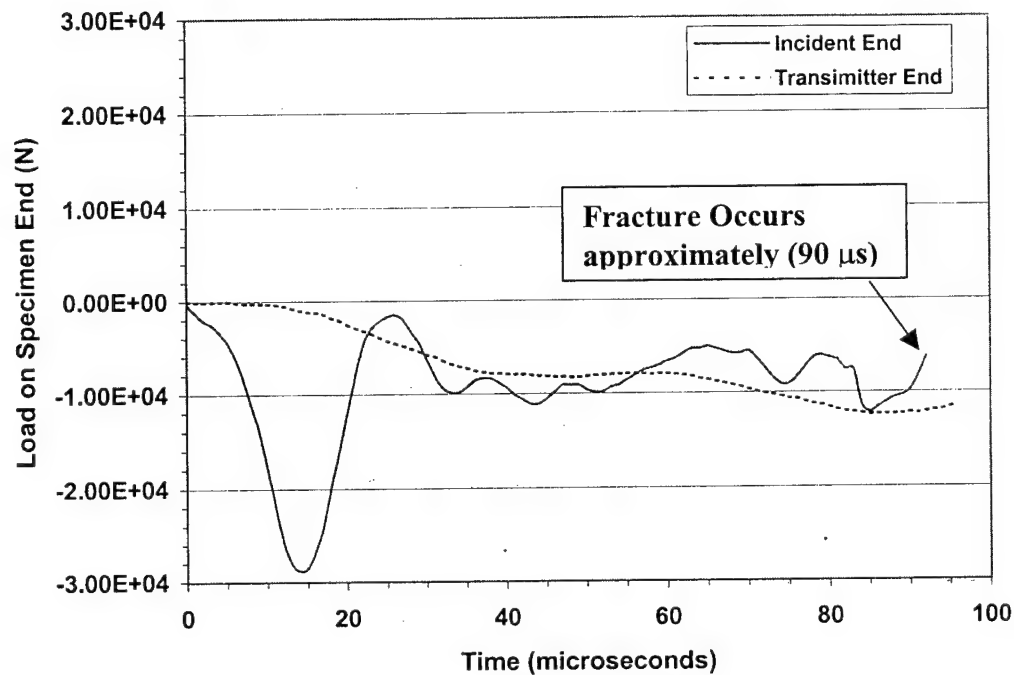
Figure 10. SHPB Contact Face Loads as a Function of Time For a Dynamic Splitting Test on a Homalite-100 Disc (HDS09)

In order to validate the contact load calculation using the SHPB strain gages, the loads are currently being determined using the photoelastic technique discussed earlier. For this work the photoelastic images recorded using the high-speed digital camera will be analyzed to determine the contact load at that time. The loads will then be compared to the strain gage load data for validation.

2.5.2.3 Crack Propagation and Failure

As demonstrated in the photoelastic analysis, a short time after initial loading the specimens reach an equilibrium condition and the stress level increases as the energy from the input pulse is pumped into the specimen by continuous reflection of the wave. As the stress reaches the failure limit in the material a crack forms and propagates across the specimen. As shown in Figure 11, failure occurs in tensile splitting along the loading line of the specimen, which is identical to the failure mechanism observed in the concrete and granite splitting experiments performed both statically and dynamically at the University of Rhode Island [3].
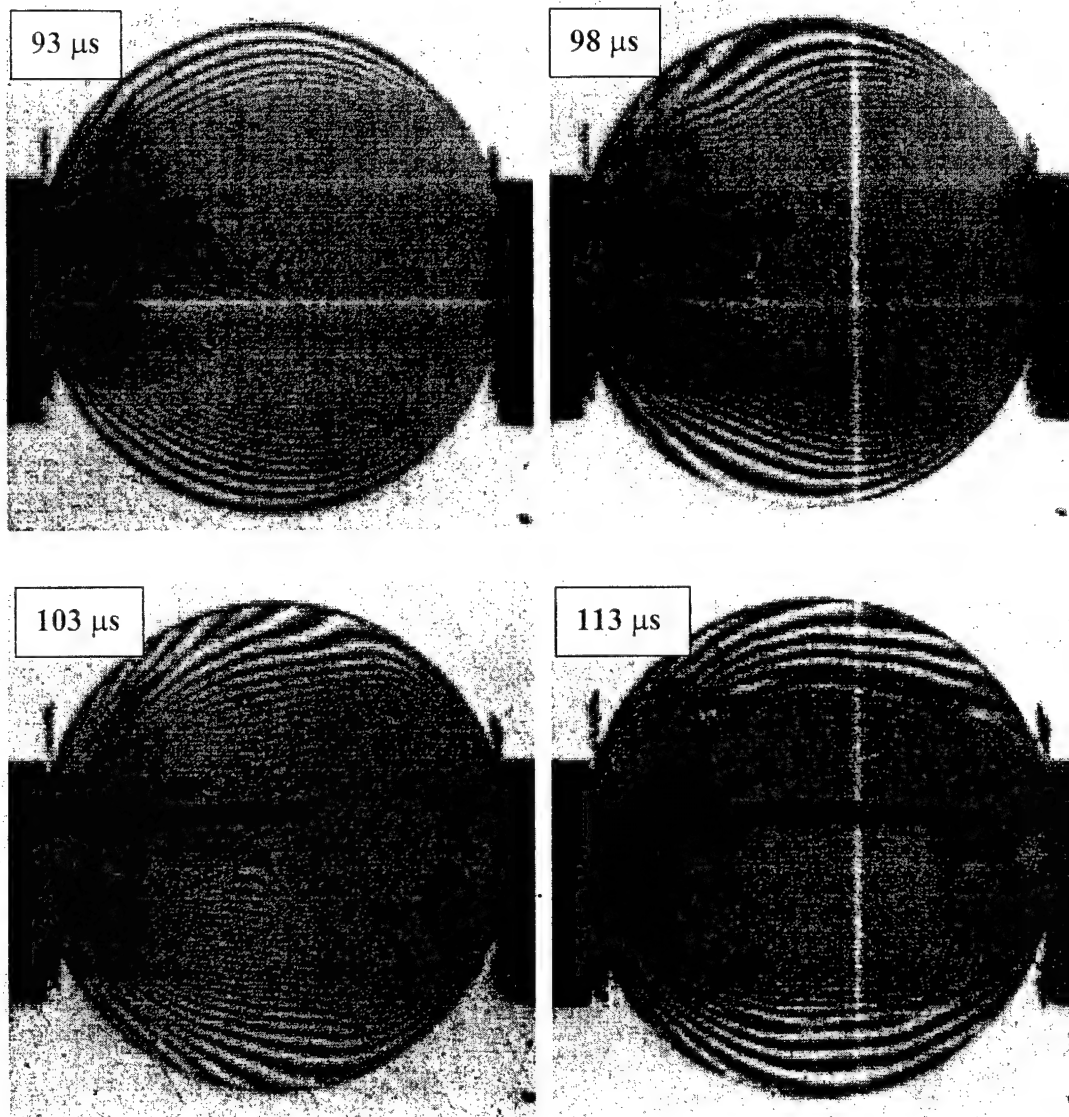
Figure 11. Crack Propagation Across Homalite-100 Disc During Dynamic Splitting Experiment (HDS13)

Cracks through the thickness of the specimen formed just outside a region of high compression at the contact points. One or more of these cracks are observed to propagate across the mid plane of the specimen. From the photographs, the position and velocity of a typical crack were calculated and plotted in Figure 12. Once formed, the crack accelerated across the disc reaching speeds up to 750 m/s, or about 60% of the shear wave velocity in Homalite-100.
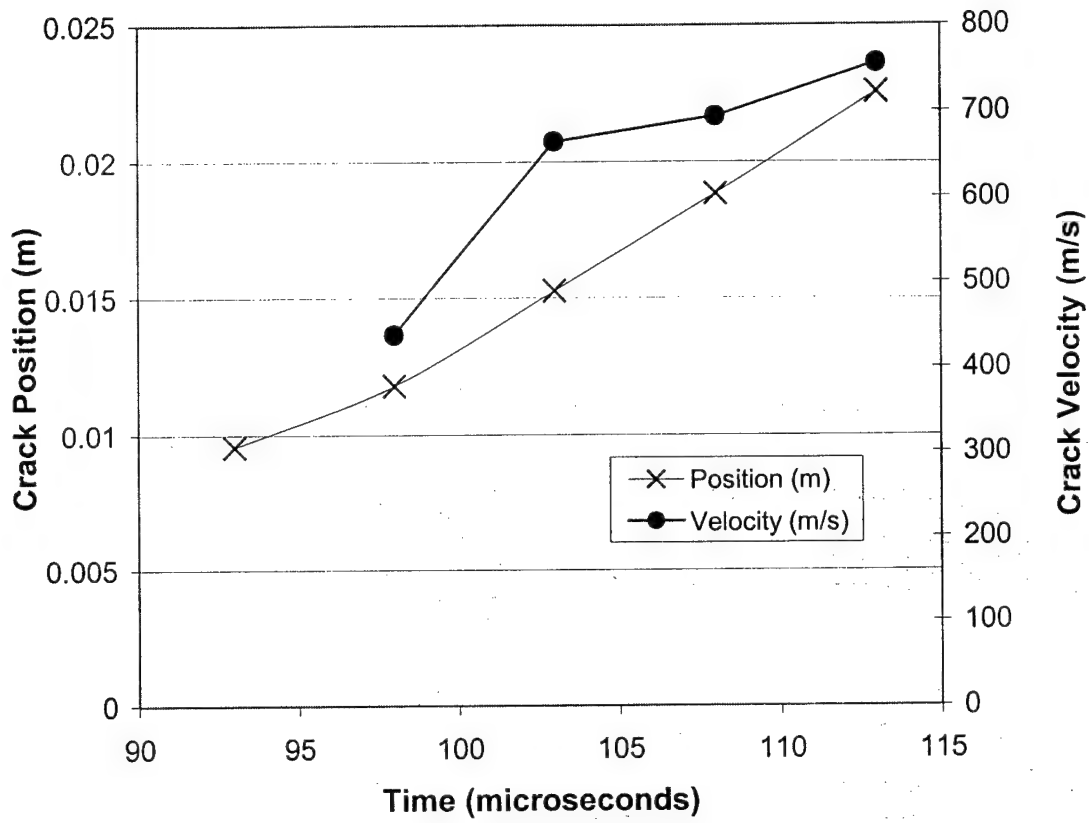
Figure 12. Crack Position and Velocity in Homalite-100 Disc During Dynamic Splitting Experiment (HDS13).

The dark regions seen growing from each contact face are also cracks, however they lie in the plane of the disc. These cracks emanate from two separate points at each contact, and then propagate toward the disc surface. Figure 13 shows a fractograph of the failed specimen in which the crack surface of the in-plane cracks can be seen curving from the contact points to the surface. This is consistent with the observed stress fields for disc contact with hard inter-particle cement, where areas of high stress develop at the two ends of the contact line [12]]. Modeling the steel bars as hard cement material, the in plane cracks form at the ends of the contact line, or in regions of high stress. These cracks then propagate outward, curving toward the disc surface. The main splitting

40

cracks actually form outside a small region around the contact point, and then travel

down the loading line of the specimen.
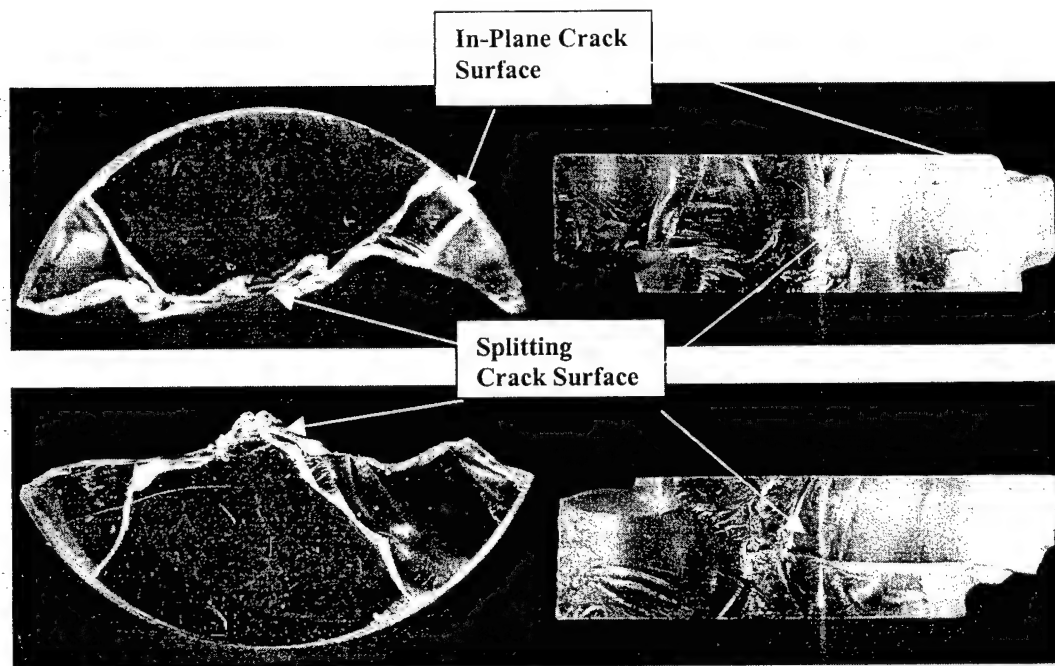
Figure 13. Fractography of Failed Tensile Splitting Homalite-100 Specimens, Front
View and Crack Surface View

The stress fields in the splitting tensile experiment can be used to explain this

fracture pattern. As previously mentioned there exists a state of high biaxial compression

at the contact points. This compression prevents the tensile splitting crack from forming

near the contact point. The tensile splitting crack will thus form a small distance away

from the contact point in a region where the compressive stress has decreased. Once

formed the crack propagates along the loading line where the maximum tensile stress is

developed. The in-plane cracks may be formed by a Poisson's effect from the high

compressive stresses at the contacts. As these cracks propagate away from the contact,

they curve outward to the surface following the rapidly decreasing compressive stress field.

2.5.2.4   Strain Rate Effect on Splitting Strength

Since Homalite-100 is a polymer, it would be expected to exhibit some time dependent behavior. Figure 14 shows the splitting strength of Homalite-100 to increase with increasing strain rate up to 55 MPa, almost twice the static splitting strength of 29 MPa. For this plot, the strain rate was calculated from the slope of the strain pulse recorded in the SHPB transmitter bar [2].
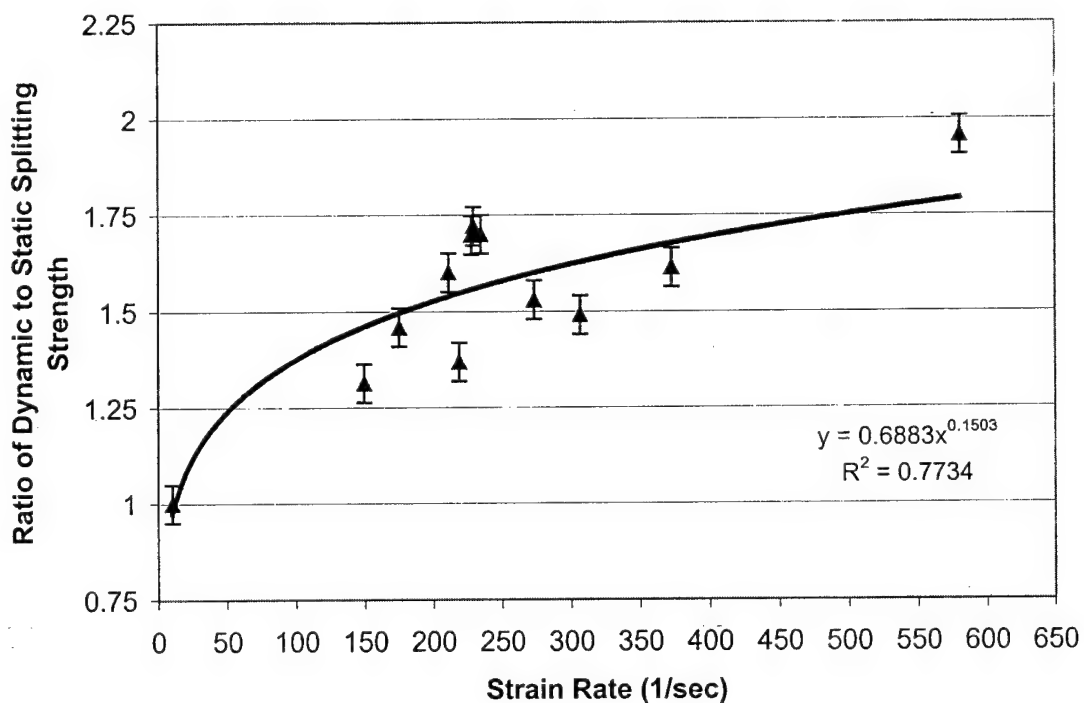
Figure 14. Strain Rate Effect on the Splitting Strength of Homalite-100

42

2.6 CONCLUSIONS

The dynamic tensile splitting experiments performed using Homalite-100 discs allowed the visualization of dynamic stress field development and specimen failure. The experiments determined that the specimens were at an equilibrium condition for a relatively long period of time prior to failure. This condition allows the used of SHPB strain gage data to calculate the load at which the specimen failed, and the static relation to calculate the splitting stress. The SHPB loads calculated at a given time also agreed well with the loads determined from the photoelastic fringes captured with a high-speed digital camera. In addition, crack velocities up to 750 m/s, or 60% of the Homalite-100 shear wave velocity, were observed as the crack propagated along the loading line of the specimens. Finally, the dynamic splitting strength of Homalite-100 was shown to increase up to approximately twice that of the static value at high strain rates.

2.7 REFERENCES

1.   Malvern, L.E., Jenkins, D.A., Tang, T., and Gong, J.C., "Dynamic Testing of Concrete with the Split Hopkinson Pressure Bar", *Proceedings of the Fourth International Symposium on the Interaction of Non-Nuclear Munitions with Structures*, Panama City, Florida, pp. 296-301, April (1989).

2.   Ross, C. A., Thompson, P. Y., and Tedesco, J. W., "Split-Hopkinson Pressure-Bar Test on Concrete and Mortar in Tension and Compression", *ACI Materials Journal*, Vol. 86, No. 5, pp. 475-481, September-October, 1989.

3.   Gomez, J. T. and Shukla, A., "Static/Dynamic Behavior of Concrete and Granite with Induced Damage", to be presented at Society of Experimental Mechanics IX International Congress, Orlando, June 2000.

4.   ASTM D3967, Splitting Tensile Strength of Cylindrical Rock Specimens

5.   ASTM C496, Splitting Tensile Strength of Cylindrical Concrete Specimens

6. Timoshenko, S. P. and Goodier, J. N., *Theory of Elasticity*, McGraw Hill, Inc., New York, Third Edition, 1987.

7. Neville, A. M., *Properties of Concrete*, Pitman Publishing, London, 1973.

8. Shukla, A., and Nigam, H., "A Numerical-Experimental Analysis of the Contact Stress Problem", *Journal of Strain Analysis*, Vol. 20, No. 4, pp. 241-245, 1985.

9. Sanford, R. J., and Dally, J. W., "A General Method for Determining Mixed Mode Stress Intensity Factors from Isochromatic Fringe Patterns", *Engineering Fracture Mechanics*, Vol. 11, pp. 621-633, 1979.

10. Kolsky, H., *Stress Waves in Solids*, Dover Publications Inc., New York, 1963.

11. Shukla, A., and Damania, C., "Experimental Investigation of Wave Velocity and Dynamic Contact Stresses in an Assembly of Discs", *Experimental Mechanics*, Vol. 27, No. 3, pp. 268-281, 1987.

12. Sienkiewicz, F., Shukla, A., Sadd, M., Zhang, Z., Dvorkin, J., "A Combined Experimental and Numerical Scheme for the Determination of Contact Loads Between Cemented Particles", *Mechanics of Materials*, Vol. 22, pp. 43-50, 1996.

CHAPTER 3   STATIC/DYNAMIC BEHAVIOR OF CONCRETE AND GRANITE IN TENSION WITH INDUCED DAMAGE

3.1 ABSTRACT

A series of dynamic and static tensile-splitting experiments were performed on concrete and granite specimens to investigate the effect of induced damage on their tensile strength.   These experiments were performed as part of a larger effort investigating the penetration process into the two materials.   The strain rate each specimen was subjected to remained constant for these experiments, while the level of induced damage was increased.   Damage was induced into the specimens through repeated drop-weight impacts and quantified using a statistical technique.   The dynamic splitting experiments were performed using a Split Hopkinson Pressure Bar (SHPB), while the static splitting experiments were conducted per the ASTM standard procedures D3967 and C496.   As part of the investigation, photoelastic dynamic tensile-splitting experiments were also performed to establish the validity of using static relations for the determination of dynamic tensile strength.   The experiments showed that the static splitting strength was highly dependent on the orientation of the induced damage with regard to the applied loading, however the dynamic tensile strength decreased with increasing damage with no apparent dependency on the random damage orientation.   An ongoing photoelastic experimental investigation is continuing to examine the insensitivity of dynamic splitting strength to damage orientation.

3.2 INTRODUCTION

This experimental study of the dynamic behavior of concrete and granite with induced damage is a portion of a larger study into the multiple impact penetration of these materials.   During the penetration process caused by multiple impacts, damage is accumulated in the region around the impact zone.   The strength of cemented materials is a function of the inherent flaws present throughout the materials [1].   By inducing damage into a material, the inherent flaws will grow in size and number, and the strength should decrease.   Therefore, it becomes important to understand the effect of damage on dynamic material strength in the study of multiple impact penetration.

To study the effect of induced damage on the strength of the G-mix Air Force concrete and Barre granite materials, damage was induced into the specimens by repeatedly dropping a weight onto the face of each specimen.   The amount of specimen damage was quantified by a measure of the crack surface area created by the damage.

Photographs of the specimens were taken before and after the damage was induced. A grid of test lines was superimposed on the damaged specimen photograph, and the intercepts of the visible cracks with the grid lines were counted. The crack surface area per specimen volume was calculated using a statistical microscopy technique [2].

The quasi-static tensile-splitting strengths of the damaged and undamaged specimens were determined using ASTM standard procedures for both the concrete and granite specimens.

To determine the dynamic tensile-splitting strength as a function of damage, a Split Hopkinson Pressure Bar (SHPB) was used to load the specimens diametrically with a dynamic stress wave. For these experiments it is assumed that the peak tensile splitting stress of the specimen can be calculated from the peak transmitted compressive strain measured in the transmitter bar using the static relationships [3]. To ensure the validity of this assumption, photoelastic dynamic-tensile splitting experiments were performed on brittle, transparent polymer discs made of Homalite-100.

The photoelastic experiments showed that the specimens were in equilibrium, i.e. the opposing contact loads were equal, for a relatively long period of time prior to failure. Also the experiments determined that once in equilibrium, the dynamic stress field in the specimen is identical to the stress field in a statically loaded specimen.

The experimental results showed that both the concrete and granite static tensile-splitting strength randomly decreased as the damage was increased, and in some cases remained unchanged in highly damaged specimens. In contrast, the dynamic tensile splitting strength of the concrete and granite decreased in an orderly manner as the level of damage was increased. These results are due the random orientation of the specimen

46

in the loading apparatus. The static spitting strength was highly dependent on the damage orientation while the dynamic splitting strength was not. An ongoing photoelastic experimental study is investigating this phenomenon.

3.3 EXPERIMENTAL PROCEDURE

3.3.1 Quasi-Static Tensile Splitting Experiments

ASTM standard Brazilian, or Tensile Splitting Experiments, are usually performed on concrete or rock [4, 5]. For these types of materials it is difficult to fabricate and test typical "dog bone" specimens. The Brazilian tensile test was developed in order to indirectly determine the tensile strength of brittle materials using cylindrical specimens. Based on elasticity theory, the two-dimensional stress field in the disc can be derived and then simplified to examine only the stress along the loading line [6]. Taking into account the specimen thickness, L, the stress distribution for the Brazilian splitting test is given by Equation 1, with parameters defined in Figure 1. [1]
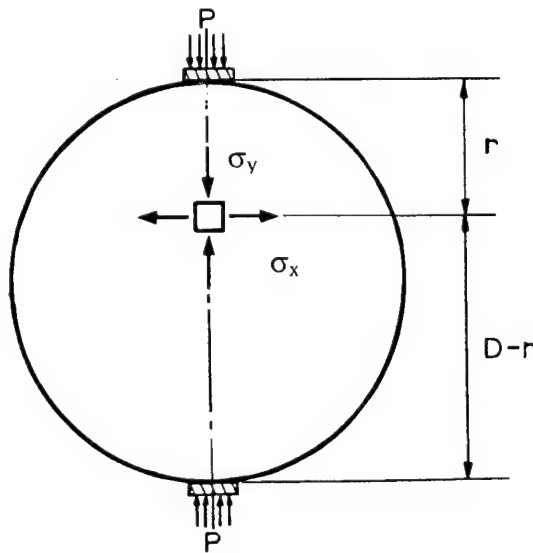
$$\sigma_y = \frac{2P}{\pi LD}\left[\frac{D^2}{r(D-r)} - 1\right] \qquad (1a)$$

$$\sigma_x = \frac{2P}{\pi LD} \qquad (1b)$$

Figure 1. Tensile-Splitting (Brazilian) Test Schematic [1]

47

As shown, a constant tensile stress, σ_x, is generated along the loading line. At the contact points the elasticity solution is no longer valid due to the singularity of the loading. At these points there exists a bi-axial compressive stress of equivalent levels, which along with the bearing blocks used to apply the load, allow the specimen to fail in tension along the loading line and not locally by compression. Brittle materials with a relatively low tensile strength compared to their compressive strength, will tend to fail in tension along the loading line. For each of the splitting tensile experiments the maximum load, P, was used to calculate the splitting stress, σ_x, at failure using Equation 1b.

3.3.2   *Split Hopkinson Pressure Bar for Tensile-Splitting*

In order to perform tensile splitting experiments under dynamic loading, a Split Hopkinson Pressure Bar (SHPB) was used in compression. However, instead of sandwiching the specimen lengthwise, the specimen was held diametrically between the bars using steel bearing bars to avoid local failure due to the point load (Figure 2).
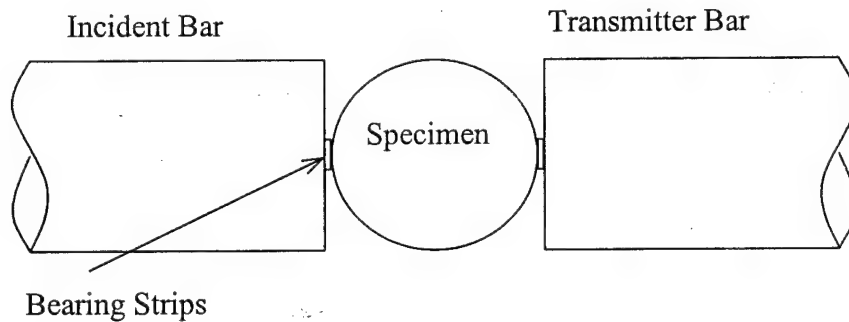

Figure 2. Dynamic Splitting (Brazilian) Experimental Setup in SHPB

To load the specimen, the incident bar is impacted with a projectile fired from a gas gun, which creates a compressive wave traveling down the bar. At the specimen, this wave will be partially reflected back into the incident bar and partially transmitted into

the transmitter bar. Strain gages mounted at the mid points of both bars are used to record the strain waves. Assuming one-dimensional propagation, and negligible attenuation of the waves, the loads on each end of the specimen can be calculated as a function of time with equations 2a and 2b. [7]

$$P_1 = A_b E_b \left(\varepsilon_i + \varepsilon_r \right) \tag{2a}$$

$$P_2 = A_b E_b \varepsilon_t \tag{2b}$$

Where P_1 and P_2 are the loads on the incident and transmitted bar contact faces respectively, A_b is the bar cross sectional area, E_b is the bar material Young's modulus, and ε_i, ε_r, ε_t are the incident, reflected, and transmitted strain pulses shifted in time to account for the mid bar location of the strain gages.

For specimens in compression, the SHPB analysis assumes that the load on each specimen face is equal, so that the specimen is in equilibrium. With this assumption the specimen stress/strain response can be calculated [7]. However, for the dynamic splitting experiment the standard analysis to obtain the specimen stress can no longer be used. For these experiments it has been assumed that the peak tensile-splitting stress of the specimen is proportional to the peak transmitted compressive strain measured in the transmitter bar by Equation 1b [3], and that the load P is now defined by Equation 2b.

For all these experiments, a 50.8 mm diameter SHPB and 406.4 mm long projectile were used. The concrete specimens were approximately 50.8 mm in diameter and 21.8 mm long. The granite specimens were approximately 55.1 mm in diameter and 31.8 mm long.

3.3.3 Photoelastic Dynamic Tensile-Splitting Experiments

Photoelastic dynamic tensile-splitting experiments were performed on a brittle transparent material, Homalite-100, to determine the validity of using the static relations for dynamically loaded specimens (Figure 3). For the static relation to be valid, the specimen must be in equilibrium, i.e. the opposing contact loads must be equal. In similar experiments involving dynamic wave propagation in a chain of discs, it was shown that if the loading pulse width is much longer than the disc diameter, quasi-static stress field equations were valid in a region close to the contact point [8]. For the SHPB dynamic loading in this study, the incident pulse length is related to the projectile length. Therefore, all the photoelastic experiments were performed on a 12.7 mm SHPB using a 203 mm long projectile, giving a strain pulse of approximately 406 mm in length. The gas gun pressure was initially varied from 0.207 MPa to 0.414 MPa to determine the pressure required to obtain fracture in the specimen. The specimens for all the dynamic splitting experiments were Homalite-100 discs, 25.4 mm in diameter and 6.4 mm thick.

Incident bar   Homalite-100 disc

High Speed
CCD Camera

Light source

Transmitter
bar

Circular
Polarizers
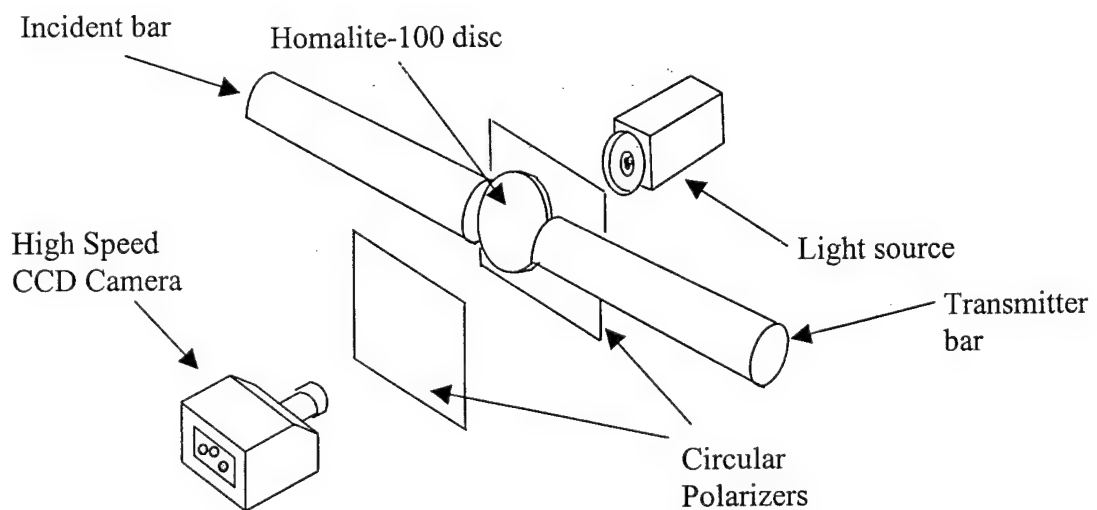
Figure 3. Schematic of Photoelastic Dynamic Tensile-Splitting Experiment

50

3.3.4   Induced Damage Application and Quantification

The concrete and granite specimens were tested both statically and dynamically as discussed earlier with increasing levels of induced damage. To induce damage into the specimens, a steel weight was dropped through a vented plastic tube, onto the specimen face. Each specimen was hit with multiple impacts until cracks were visible in the specimen face.

The amount of specimen damage was quantified by a measure of the crack surface area created by the damage. Photographs of the specimens were taken before and after the damage was induced. A grid of test lines was superimposed on the damaged specimen photograph, and the intercepts of the visible cracks with the grid lines were counted. The crack surface area per specimen volume, S_V, is proportional to the number of intercepts by:

$$S_v = \frac{2N}{L_{ts}} = \frac{2 \text{ (number of intercepts)}}{\text{Test line length}} \tag{3}$$

This method was originally developed as a microscopy technique to study the flaws and grain boundaries of metal samples [2].

For all the experiments, static and dynamic, no particular specimen orientation of the damage to the loading line was desired. The specimens were randomly oriented between the loading contacts.

3.4 RESULTS AND DISCUSSION

3.4.1 *Specimen Equilibrium*

The photoelastic experiments determined that by subjecting the splitting specimen to a relatively long dynamic loading pulse in the SHPB, the specimen reaches equilibrium quickly and remains in equilibrium until fracture occurs. As shown (Figure 4), the wave front enters the specimen, loading only the incident contact (0 s). Both contact points of the specimen begin to be loaded when the wave travels across the specimen (10 s). When the contact loads become equal (30 s) the specimen is in equilibrium, and the photoelastic fringe patterns appear identical to a statically loaded specimen (Figure 5). These fringe patterns are lines of constant maximum shear stress, and can be used to determine the stress fields in the specimens. [9]
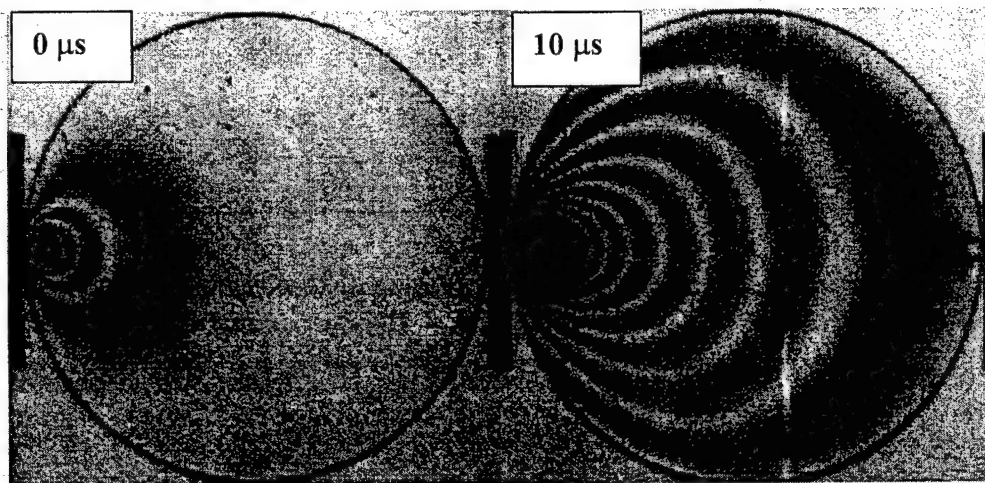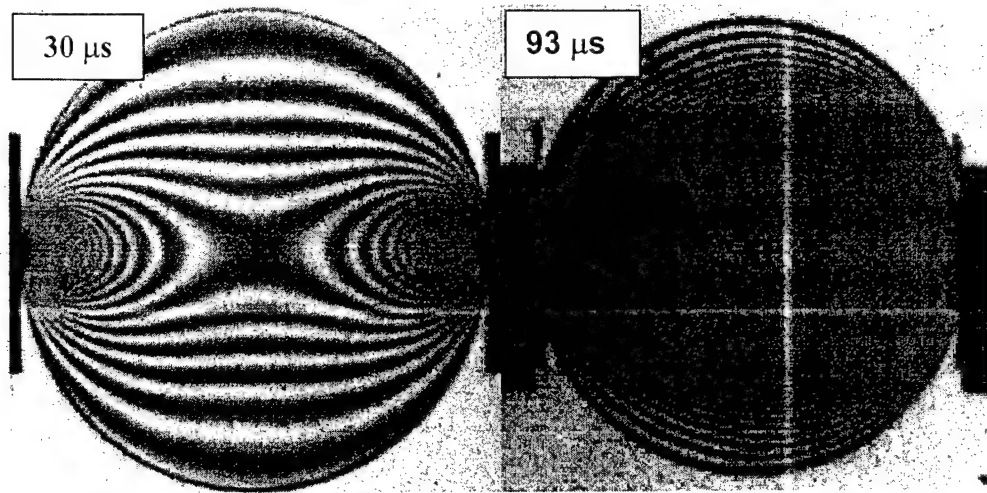
Figure 4. Homalite-100 Specimen in Dynamic Tensile-Splitting Experiment
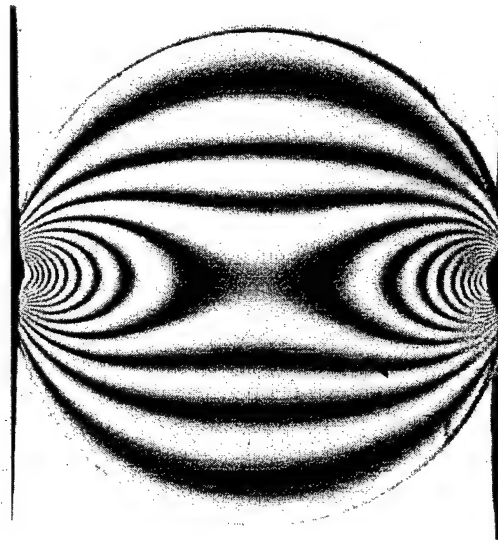
Figure 5. Static Homalite-100 Tensile-Splitting Fringe Pattern

From this result, the specimen was shown to be in equilibrium at the time of failure, and the stress field appears identical to the static stress field. With this, the static relations are valid to determine the dynamic splitting strength of a specimen loaded in a SHPB with a relatively long projectile.

3.4.2 Static Tensile-Splitting Results

As shown, the static splitting strength of both the concrete (Figure 6) and the Granite (Figure 7) as a function of damage randomly decreases to about half its virgin strength as the damage increases. However, in some cases the material retained its full strength even though the specimen was highly damaged.
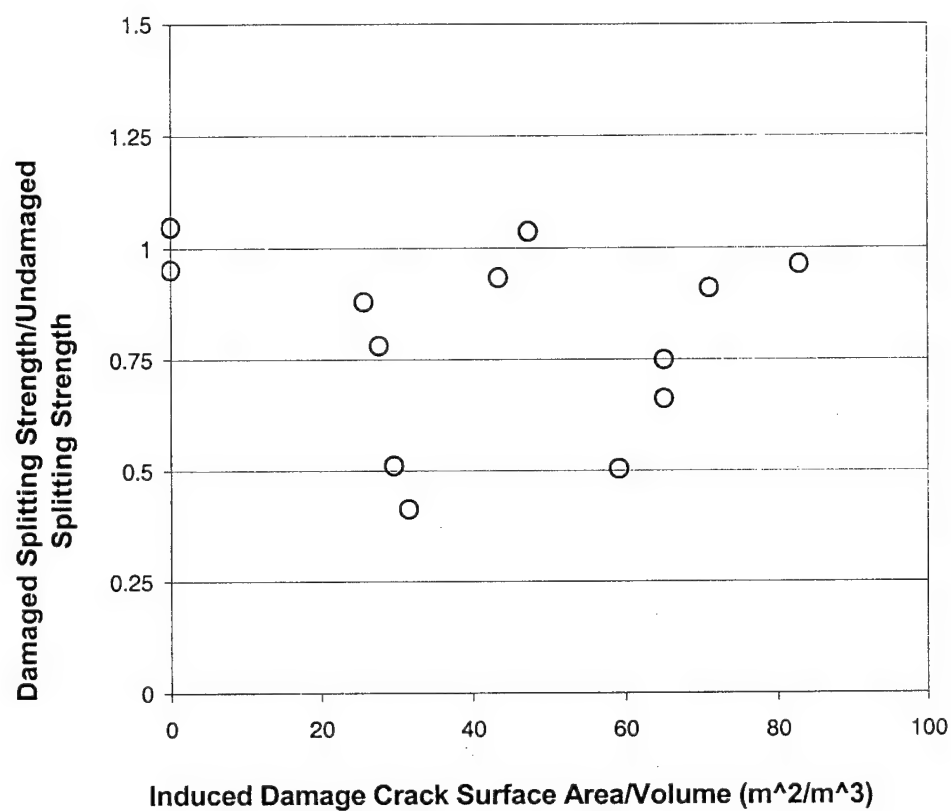
Figure 6. Static Splitting Strength of G mix Concrete as a Function of Induced Damage
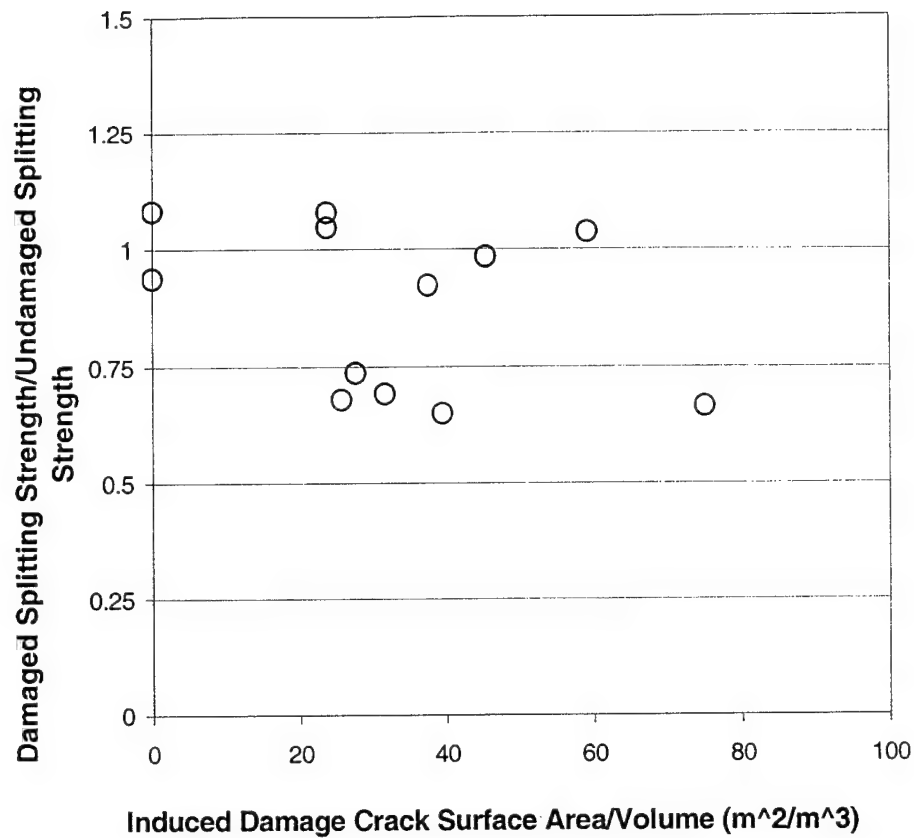
Figure 7. Static Splitting Strength of Barre Granite as a Function of Induced Damage

This is a result of the slowly developing stress field being dependent on the damage orientation with respect to the loading line. As mentioned, the tensile splitting test develops a constant tensile stress down the loading line of the specimen. If the damage cracks were parallel to the loading line, they would greatly decrease the strength. However, if the damage cracks were perpendicular to the loading line, the cracks would close under the compression in the y direction and not affect the splitting strength. This dependency on random damage orientation is evident in the static splitting results.

3.4.3 Dynamic Tensile-Splitting Results

As shown, the dynamic splitting strength for both the concrete (Figure 8) and granite (Figure 9) decrease in an orderly fashion with increasing damage. This result shows that the random orientation of damage cracks in the specimens does not affect the dynamic splitting strength as it did in the static experiments.
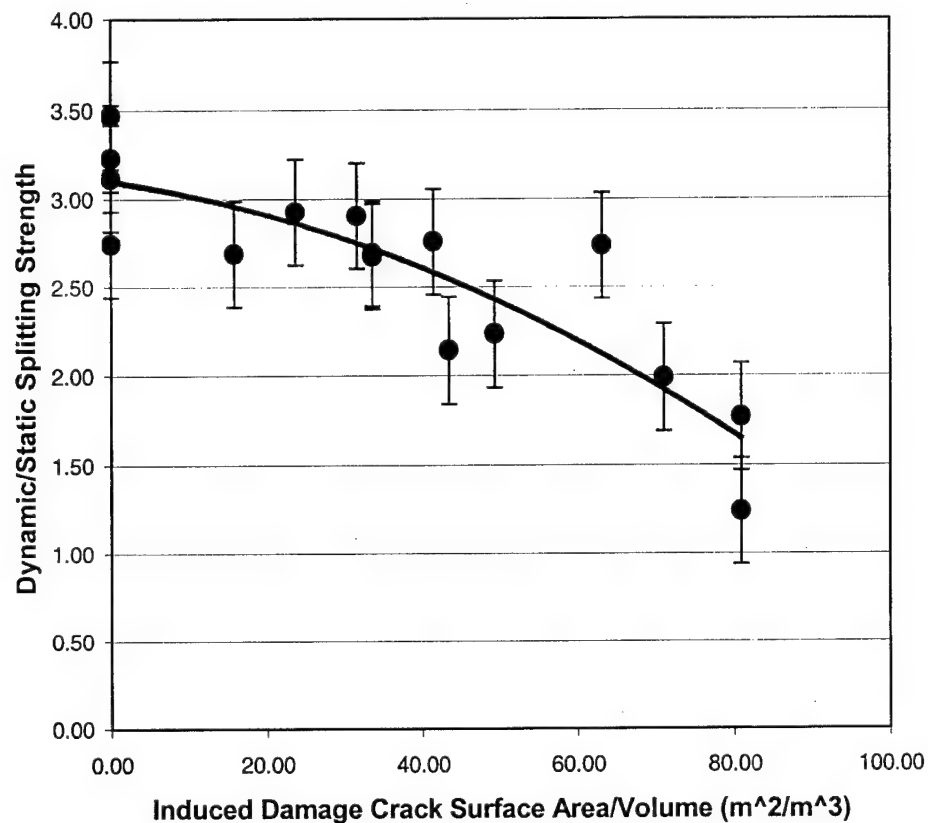

Figure 8. Dynamic Splitting Strength of G mix Concrete as a Function of Induced Damage
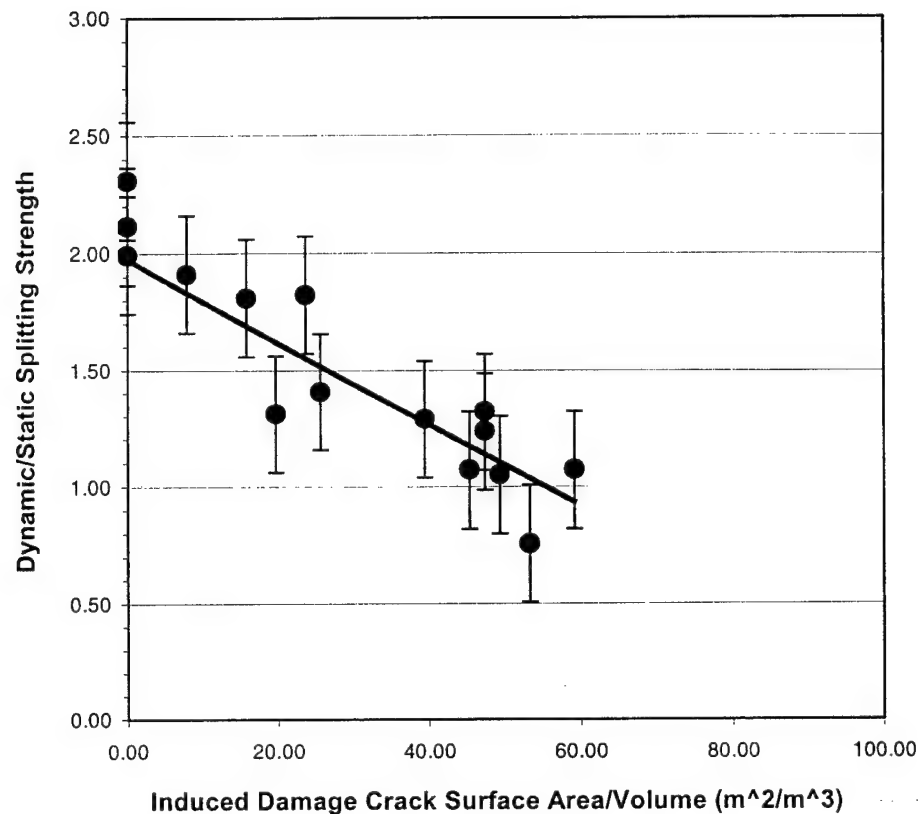
Figure 9. Dynamic Splitting Strength of Barre Granite as a Function of Induced Damage

3.5 CONCLUSION

The static and dynamic tensile-splitting experiments performed determined the effect of induced levels of damage on the splitting strength of concrete and granite specimens. The static experiments showed that the splitting strength is highly dependent on the orientation of the damage with respect to the loading line.

In the dynamic case, the photoelastic experiments determined that the specimens were in equilibrium, and the dynamic stress field resembled the static stress field. This allows the use of the static stress field relation to calculate the dynamic splitting strength.

For the concrete and granite specimens, the dynamic splitting strength was shown to decrease in a regular fashion with increasing damage without a dependency on the

damage orientation. An ongoing photoelastic investigation is continuing to study this result.

3.7 REFERENCES

1. Neville, A. M., *Properties of Concrete*, Pitman Publishing, London, 1973.

2. Underwood, E. E., "Surface Area and Length in Volume", *Quantitative Microscopy*, McGraw-Hill, pp. 78-125, 1968.

3. Ross, C. A., Thompson, P. Y., and Tedesco, J. W., "Split-Hopkinson Pressure-Bar Test on Concrete and Mortar in Tension and Compression", *ACI Materials Journal*, Vol. 86, No. 5, pp. 475-481, September-October, 1989.

4. ASTM C496, Splitting Tensile Strength of Cylindrical Concrete Specimens.

5. ASTM D3967, Splitting Tensile Strength of Cylindrical Rock Specimens.

6. Timoshenko, S. P. and Goodier, J. N., *Theory of Elasticity*, McGraw Hill, Inc., New York, Third Edition, 1987.

7. Kolsky, H., *Stress Waves in Solids*, Dover Publications Inc., New York, 1963.

8. Shukla, A., and Damania, C., "Experimental Investigation of Wave Velocity and Dynamic Contact Stresses in an Assembly of Discs", *Experimental Mechanics*, Vol. 27, No. 3, pp. 268-281, 1987.

9. Shukla, A., and Nigam, H., "A Numerical-Experimental Analysis of the Contact Stress Problem", *Journal of Strain Analysis*, Vol. 20, No. 4, pp. 241-245, 1985.

CHAPTER 4   MULTIPLE IMPACT PENETRATION EXPERIMENTS OF SEMI-INFINITE CONCRETE

4.1 INTRODUCTION

The military's interest in using geo-materials as an ordinance barrier has provided the motivation for studying projectile impact into concrete since the mid 1700's. The interest lies in both the development of projectiles capable of penetrating barriers and the barriers capable of withstanding penetration. The bulk of the early work through the 1800's consisted of experimental studies with a wide range of projectile sizes and striking velocities from 200 to 1000 m/s. These studies present graphical results of data such as penetration, perforation, crater formation, ricochet, and the effect of reinforcement for different impact velocities and angles [1, 2]

Starting in the 1940's Government laboratories, such the Ballistic Research Laboratory (BRL) and the Waterways Experimental Station (WES), began gathering experimental concrete penetration data for the development of empirical formulas [3]. Most recently researchers from Sandia National Laboratories (SNL) have performed numerous impact penetration studies on soil and concrete targets to gather experimental data required to develop some physics based, semi-empirical models to predict penetration [4]

All of the previous penetration studies of concrete have been conducted with a single projectile fired into virgin material, examining the effect of velocity, or projectile geometry on target penetration. In addition to the effect of velocity on penetration depth, the study conducted here examined the effect of multiple projectile impacts on the

penetration of concrete. With multiple projectiles impacting the same point in a target, the accumulation of damage and crater formation with each impact become important to the overall penetration depth. This experimental study was conducted to gather data for penetration depth and crater formation in semi-infinite concrete targets as a function of multiple projectile impacts. The data was intended for use in understanding the multiple impact penetration process, and developing a semi-empirical model capable of predicting penetration depth.

4.2 EXPERIMENTAL SET-UP

4.2.1 Projectile Impact: Vertical Gun Setup

To perform the impact testing a Remington Model 700, 30-06 rifle was mounted vertically above a steel test chamber. The rifle was slightly modified to allow remote operation. Figure 4.1 shows the rifle and test chamber set up.
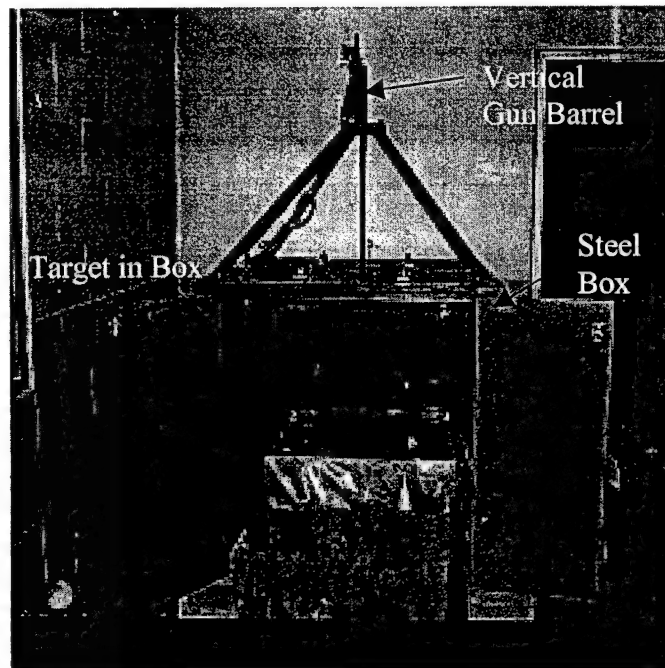
Figure 4.1. Vertical Gun Impact Set-up

Ogive-nose shape projectiles with a length/diameter ratio of 10 were designed and fabricated for use with the rifle test fixture. The projectiles, whose geometry is shown in Figure 4.2, were fabricated from maraging steel. The material properties of maraging steel are listed in Table 4.1. A plastic sabot, also shown in Figure 4.2, was designed and fabricated to allow the use of the 6.4 mm diameter projectile in the 7.82 mm diameter bore of the rifle. To align the rifle and target, a laser sight was mounted in the action of the rifle and the beam sent down the bore onto the target.
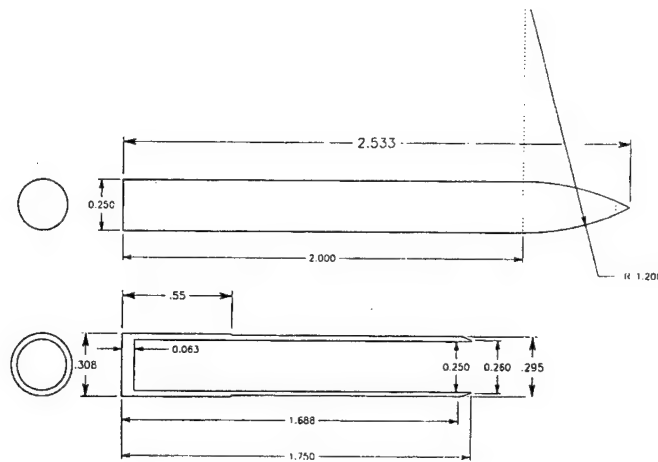
Figure 4.2. Projectile and Sabot Geometry (dimensions in inches)

Table 4.1. Material properties for marageing steel projectiles

Alloy	VASCOMAX C-300
Ultimate Strength (MPa)	2068
Yield Strength (MPa)	1999
Density (kg/m^3)	8118
Young's Modulus (GPa)	206.8
Charpy Impact (N-m)	20 (10mm)
Rockwell Hardness C	53

The semi-infinite targets were fabricated from G concrete mixed at Tyndall Airforce Base. This is the same material that was used for the static and dynamic property testing discussed earlier. Material properties for the G mix concrete are listed in Table 4.2. The 406 mm cube targets were placed in a plywood box and surrounded by wet sand. The size of the target, and the sand were an attempt to simulate a semi-infinite target by suppressing tensile stress wave reflections from the target walls resulting from the impacts. A concrete target loaded in the sand is shown in Figure 4.1 inside the steel containment chamber.

Table 4.2. Material Properties for G mix concrete

Compressive Strength (MPa)	40.5
Splitting Tensile Strength (MPa)	3
Density (kg/cubic meter)	2336.8
Mixture for one cubic yard (kg)	
3/8 - 4 limestone	757.5
Concrete Sand	592.4
Portland Cement, Type 1	164.7
Class "F" Fly Ash	108.9
Water	164.7

4.2.2 Velocity System

To measure the velocity of the projectile, a break screen system was fabricated. Two paper screens were held in a fixture a known distance apart. The screens contained a conductive coating that was included in a high-speed flip-flop circuit. Recording the circuit output on an oscilloscope, a square wave is produced as the projectile passes through the screens. A schematic of the velocity measurement system and its typical

output are shown in Figure 4.3. The schematic diagram of the flip-flop circuit is shown

in Appendix A.
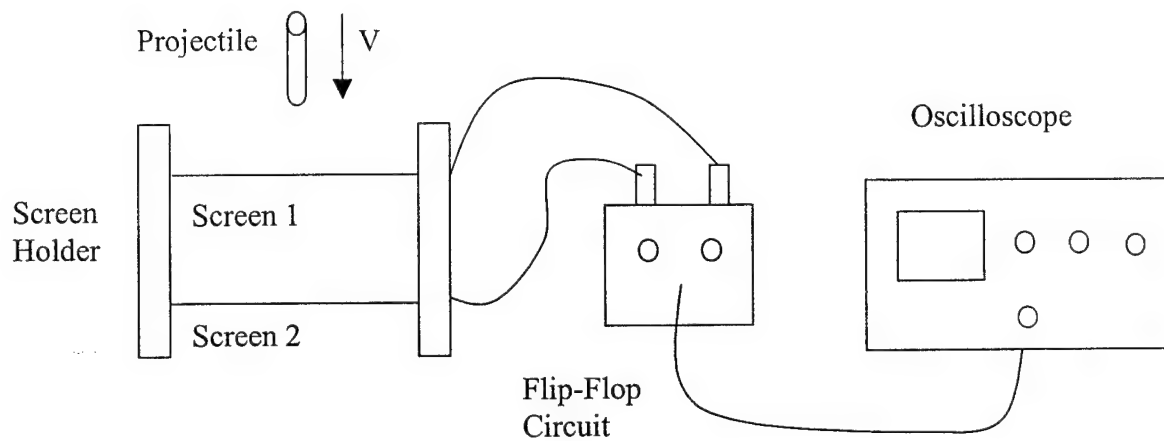
Figure 4.3a. Schematic of Velocity System

Time = 0.000236 seconds
Distance = 0.0733 meters
Velocity = 310.7 m/s
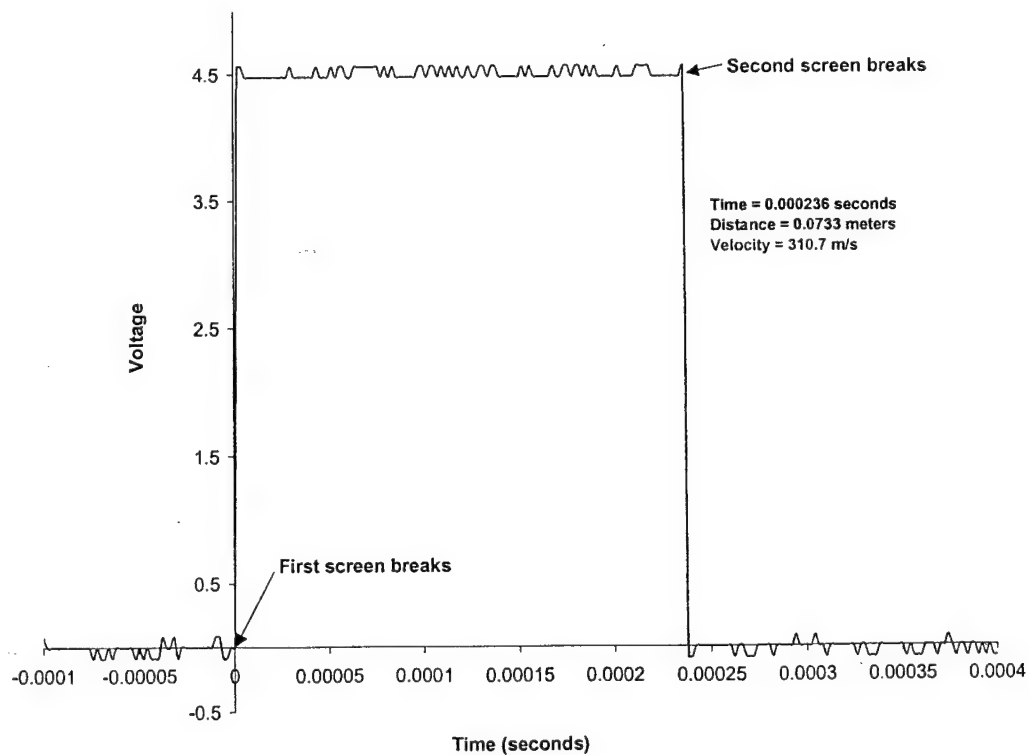
Figure 4.3b. Typical output from velocity system

4.2.3 Experimental Procedure

Projectile impacts into a particular target were conducted at a given velocity until the target failed, i.e. cracks propagated to the boundary of the cube in contact with the sand. Different velocities for each target were achieved by changing the amount of gunpowder loaded into each projectile. Figure 4.4 shows the velocity versus gunpowder load curve for the 15 gram steel projectiles generated during early calibration experiments.

The equation shown on the graph is $y = 312.17 \mathrm{Ln}(x) - 561.94$ with $R^2 = 0.9674$. The x-axis is labeled "Powder Mass (grains)" and the y-axis is labeled "Velocity (m/s)".
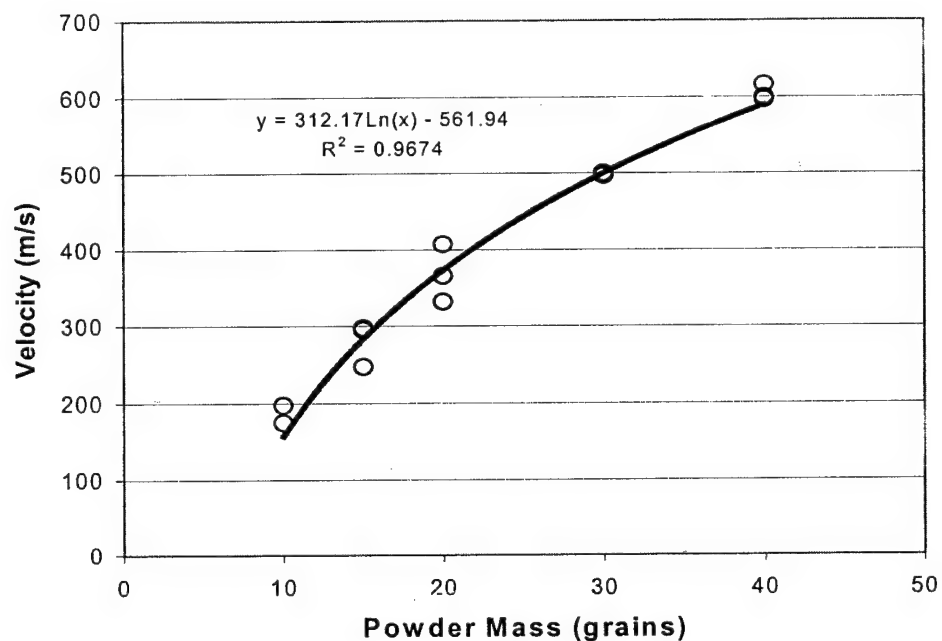
Figure 4.4. Velocity versus Gunpowder load curve for 15 gram steel projectile fired from vertical 30-06 projectile impact stand

For each experiment the projectile and sabot were hand loaded into a standard shell casing with the proper amount of gunpowder for the desired velocity using the reloading procedure listed in Appendix B. Figure 4.5 shows a loaded and unloaded bullet

Figure 4.5. Maraging steel projectile with sabot alone and loaded in shell casing
(figure not included)

Prior to loading the bullet into the gun chamber, the target was positioned in the containment chamber using the laser sight to ensure proper alignment. The velocity system screen holders were mounted to a plywood cover for the target box, and placed over the target. The cover also helped to contain the target material ejected from the crater during the experiment. Due to the small size of the containment chamber, a cardboard baffle was used to suppress the muzzle blast at the end of the gun barrel. With the target loaded and velocity system in place and operational, the containment chamber was locked and the gun fired remotely using a series of cables. The procedure developed and used to perform these experiments is listed in Appendix B.

4.3 RESULTS AND DISCUSSION

After each projectile was fired, the gun system was immediately put into a safe condition, and the velocity data recorded. Upon opening the containment chamber, the projectile was usually found imbedded into the target as shown in Figure 4.6. Along with the projectile, various amounts of material ejected from the crater was contained on the top surface of the target. The projectile was removed and the crater material collected for later examination. The primary data collected from each experiment was the overall depth of penetration.

Figure 4.6. Target condition post experiment, with embedded projectile and crater
material (figure not included)

To record penetration depth, a large parallel was placed across the crater and a probe was used to measure perpendicularly from the target surface to the bottom of the penetration tunnel. At least 6 measurements were taken and then averaged. Figure 4.7 shows the concrete penetration depth of a 15 gram maraging steel projectile for multiple shots at various velocities.
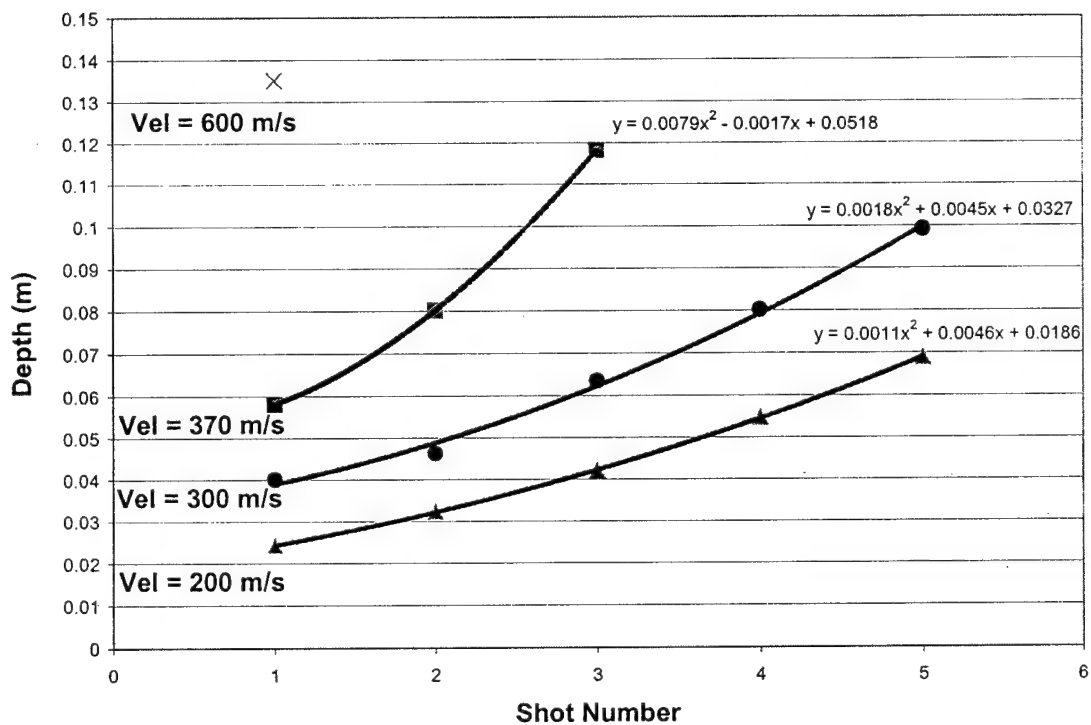
Figure 4.7. Multiple impact penetration depth for a 15 g projectile for various velocities

As shown, the depth of penetration for each subsequent shot at a given velocity increased in orderly increments. This important result implies that this penetration depth can be predicted with a model based on target properties, projectile parameters, velocity and shot number. If the penetration depths for each shot appeared random, no logical prediction of their value could be made.

66

Observation of the penetration process during these experiments show that the process consists of two parts; initial crater formation and projectile tunneling. This result is consistent with experimental results from other penetration studies [5, 6]. To study the crater formation during multiple impact penetration, the crater volume, diameter and depth were recorded following each experiment. Figures 4.8, 4.9, and 4.10 show the crater depth, volume, and diameter respectively for every penetration experiment. As shown, regardless of the velocity or shot number, once the crater was fully formed, its size remained constant.
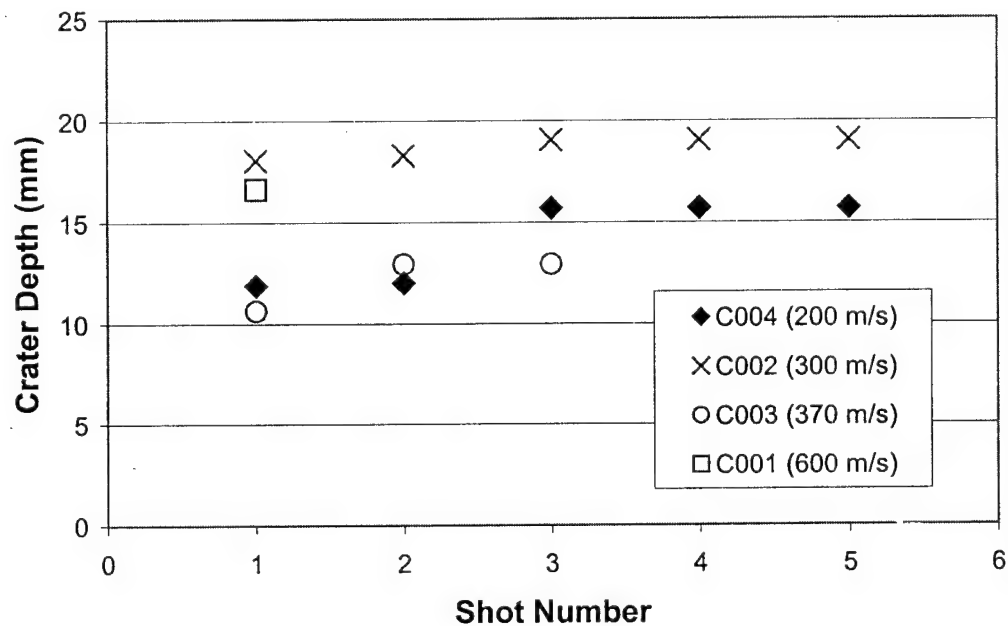
Figure 4.8. Crater depth for ogive–nose shape, multiple impact penetration into concrete
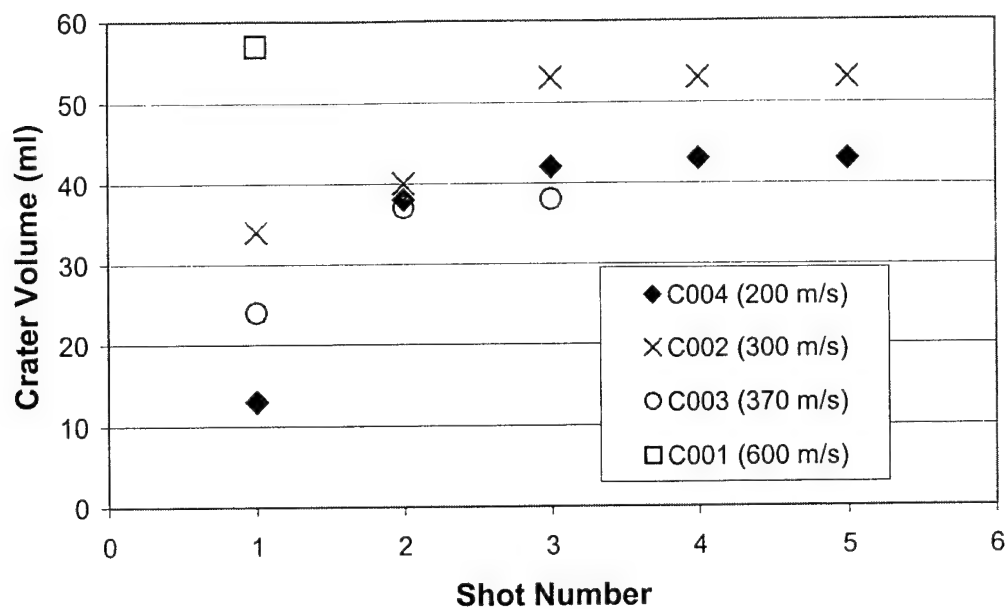
Figure 4.9. Crater volume for ogive–nose shape, multiple impact penetration into concrete
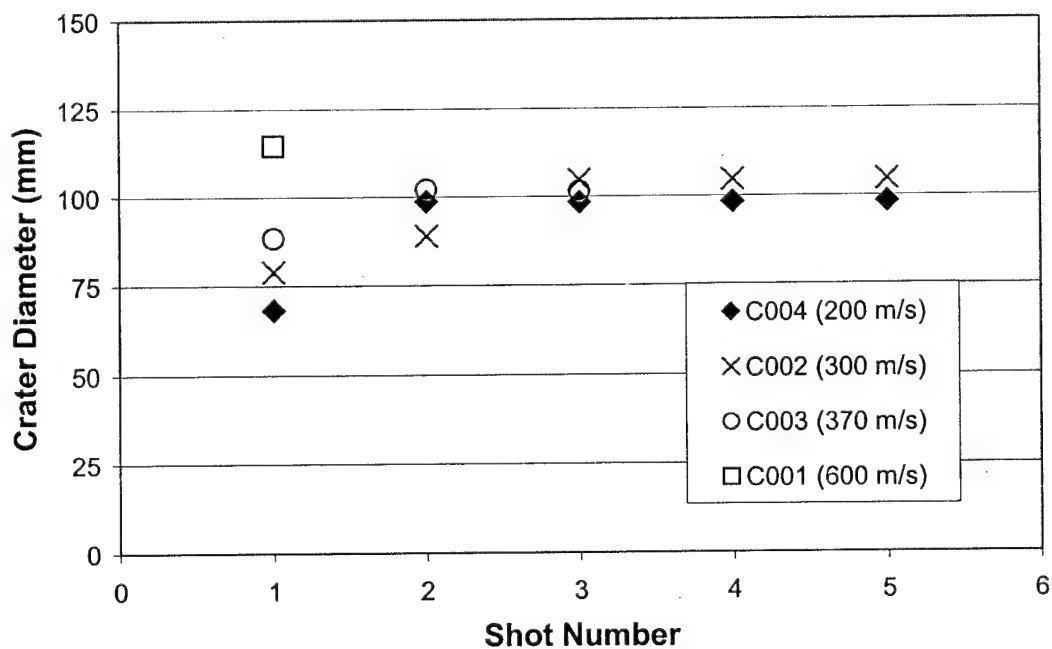
Figure 4.10. Crater diameter for ogive–nose shape, multiple impact penetration into concrete

Forrestal observed this same phenomenon while conducting soil and concrete penetration tests using similar ogive-nose projectiles [5, 6]. For Forrestal's soil penetration, the crater depth was small compared to the overall penetration, and therefore was neglected when developing a predictive model. However for the concrete penetration the crater depth was no longer negligible, and was taken as a constant value, experimentally determined as 4 times the projectile radius. In our experiments the crater depth was observed to be approximately 5 times the projectile radius, 15.5 mm.

4.4 CONCLUSIONS

The significance of the data gathered and observations made is that due to the orderly nature of the penetration depth, and crater formation, not only for single impact, but for multiple projectile impact, it appears that a predictive model can be formulated to determine the depth of penetration. With the consistency between the crater formation and tunneling between single and multiple impact penetration, it may be possible to extend an existing single impact penetration model to predict the depth of subsequent impact penetration.

4.5 REFERENCE

1.   Robinson, H. P., "Terminal Ballistics", CPPA/B, NRC, (1941).

2.   White, M. T., "Effects of Impact and Explosion. Summary Tech Report of Div 2", National Defense Research Committee, vol.1, Office of Scientific Research and Development, (1946).

3. Kennedy, R. P., "A Review of Procedures for the Analysis and Design of Concrete Structures to Resist Missile Impact Effects", Nuclear Engineering and Design, vol. 37, pp. 183-203 (1976).

4. Forrestal, M.J., Cargile, J.D., Tzou, D.Y., "Penetration of Concrete Targets", American Society of Mechanical Engineers, AMD-Vol. 171, pp. 9-16, (1993).

5. Forrestal, M. J. and Luk, V. K., "Penetration into Soil Targets", International Journal of Impact Engineering, vol. 12, pp. 427-444, (1992).

6. Forrestal, M.J., Altman, B.S., Cargile, J.D., Hanchak, S.J., "An Empirical Equation for Penetration Depth of Ogive-Nose Projectiles into Concrete Targets", International Journal of Impact Engineering, Vol. 15, No. 4, pp. 395-404, (1994).

CHAPTER 5   DEVELOPMENT OF EMPIRICAL MODEL OF MULTIPLE IMPACT PENETRATION PROCESS IN CONCRETE AND GRANITE TARGETS

5.1 INTRODUCTION

In order to develop a penetration model with a physical basis, research at Sandia National Laboratories (SNL) was begun by M. J. Forrestal to developed cavity expansion models for penetration into dry porous rock [1] and reinforced concrete [2] using the cavity expansion expressions developed earlier by Bishop [3] and Hill [4]. From these experimental studies, it appeared that the spherical cavity expansion model showed better agreement with experimental data than the cylindrical cavity expansion. This method uses the cavity expansion theory to predict the axial force on a rigid projectile as a function of velocity. With this force, the penetration depth can be determined. However, tri-axial material property data is required to calculate parameters used in the cavity expansion method.

In 1992, Forrestal *et al* conducted a study to predict penetration with a spherical cavity expansion model of soil [5]. The experimental portion of the study used large instrumented projectiles fired from a gas gun into soil for comparison with model predictions for projectile deceleration and penetration. The results again agreed well, however the model required tri-axial material testing of the soil as inputs. To eliminate the need for the tri-axial material data to describe the behavior of the target material, Forrestal *et al* (1994, 1996) and Frew *et al* (1998) developed a semi-empirical equation for the penetration of ogive-nose projectiles into concrete [6, 7, 8]. From the results of a series of concrete penetration experiments and the projectile force expressions from their

71

soil penetration work, they developed an equation that is dependent on one dimensionless constant, later shown to be a function of the target compressive strength. The equation was also used to accurately predict the penetration of large-scale projectiles from historical data.

In this study, the semi-empirical penetration models developed at SNL will be extended to predict the penetration depth of multiple projectile impacts. The multiple projectile impact data presented earlier will form the experimental basis for this work.

5.2 MULTIPLE IMPACT PENETRATION DATA

As presented earlier, penetration experiments were performed on semi-infinite G mix concrete whose properties are listed in Table 5.1. The experiments were all performed with ogive-nose shaped projectiles fabricated from maraging steel. The projectile material properties are listed in Table 5.2 and its geometry is shown in Figure 5.1.

Table 5.1. G mix concrete material properties

Compressive Strength (MPa)	40.5
Splitting Tensile Strength (MPa)	3
Density (kg/cubic meter)	2336.8
Mixture for one cubic yard (lbs)	
3/8 - 4 limestone	757.5
Concrete Sand	592.4
Portland Cement, Type 1	164.7
Class "F" Fly Ash	108.9
Water	164.7

Table 5.2. Material properties for maraging steel projectiles

Alloy	VASCOMAX C-300
Ultimate Strength (MPa)	2068
Yield Strength (MPa)	1999
Density (kg/m^3)	8118
Young's Modulus (GPa)	206.8
Charpy Impact (N-m)	20 (10mm)
Rockwell Hardness C	53
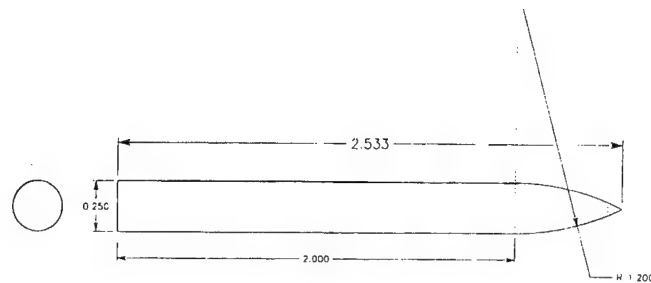
Figure 5.1. Projectile geometry (dimensions in inches)

The penetration experiments were performed at velocities ranging from 200 to 600 m/s. A single concrete target was impacted at a constant velocity multiple times until a global failure of the cube occurred. For each experiment velocity, penetration depth and crater dimensions were recorded. Table 5.3 lists the penetration data shown graphically earlier.

Table 5.3. Multiple Impact Penetration Data

Specimen	C001		C002				
Test Number	VG007		VG008	VG009	VG011	VG012	VG013
Shot Number	1		1	2	3	4	5
Projectile Mass (kg)	0.0153		0.0151	0.0144	0.0149	0.0147	0.0151
Velocity (m/s)	616		298	291	295	291	310
Penetration Depth (m)	0.13513		0.04003	0.04627	0.06348	0.08019	0.09915

Specimen	C003				C004				
Test Number	VG014	VG015	VG023		VG016	VG017	VG018	VG019	VG021
Shot Number	1	2	3		1	2	3	4	5
Projectile Mass (kg)	0.0149	0.0148	0.0149		0.0150	0.0150	0.0150	0.0150	0.0150
Velocity (m/s)	375	362	359		186	183	207	203	212
Penetration Depth (m)	0.05807	0.08019	0.11820		0.02426	0.03233	0.04199	0.05472	0.06899

5.3 DEVELOPMENT OF CONCRETE IMPACT PENETRATION MODEL

5.3.1   *Forrestal's Single Impact Penetration Model [6,7,8]*

As observed in soil penetration experiments [5], the penetration process is comprised of two components, crater formation and tunneling. The axial force, F, on the projectile ogive-nose during the tunneling region is given by

$$F = \pi a^2 (\tau_0 A + NB\rho V^2) \tag{1}$$

where a is the projectile radius, ρ is the target density, V is the projectile velocity, and N is given by

$$N = \frac{8\psi - 1}{24\psi^2} \tag{2}$$

N is a function of the Caliber Radius Head (CRH), $\psi = s/2a$, where s is the radius of the ogive-nose and a is the projectile radius shown in Figure 5.1. In equation (1), $\tau_0 A$ and B are constants that can be determined by a cavity expansion analysis.

To eliminate the cavity expansion analysis, and hence the need for tri-axial material data, $\tau_0 A$ and B can be approximated. Experimental data has shown that B has a very small range for a wide variety of materials and can be approximated as 1.0. $\tau_0 A$ can be set equal to Sf_c' where f_c' is the unconfined compressive strength of the target material, and S is a dimensionless parameter that modifies the compressive strength. With this, equation (1) becomes

$$F = \pi a^2 (Sf_c' + N\rho V^2) \tag{3}$$

During crater formation during the soil penetration study, the projectile was shown to decelerate linearly so the axial force on the projectile during is taken as

$$F = cz \tag{4}$$

where z is the penetration depth from the target surface and c is a constant. Figure 5.2 is a schematic of the penetration process.
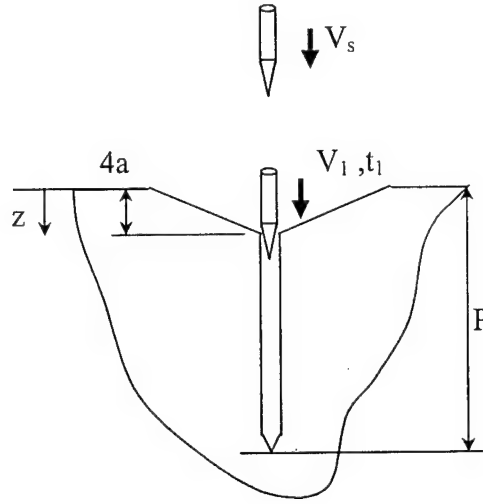
Figure 5.2. Schematic of Penetration Geometry

Therefore, equation 4 is valid for the crater formation region only, z equals 0 to $4a$, and equation 3 is valid for the tunneling region, z equals $4a$ to the final penetration depth, P. Using Newton's second law equation 4 can be written for the crater region with the initial conditions $z(0)=0$ and $V(0)=V_s$, the impact velocity.

$$m\frac{d^2z}{dt^2} = -cz, \quad 0 \le z \le 4a \tag{5}$$

Solving the differential equation gives the position z, velocity V, and acceleration on the projectile as a function of time

$$z = \left(\frac{V_s}{\omega}\right)\sin(\omega t) \tag{6}$$

$$V = \frac{dz}{dt} = V_s\cos(\omega t) \tag{7}$$

$$\frac{dV}{dt} = -\omega V_s \sin(\omega t) \tag{8}$$

where $\omega^2 = c/m$. V_1 and t_1 are defined as the velocity and time at the transition from crater to tunneling at $z=4a$. At this point there has to be continuous force, velocity, and displacement of the projectile. Using the continuity conditions, the velocity at this transition, V_1 can be determined as

$$V_1^2 = \frac{mV_s^2 - 4\pi a^3 Sf_c'}{m + 4\pi a^3 N\rho} \tag{9}$$

The final depth of penetration can now be found by again applying Newton's second law to equation 3 for the tunneling region

$$mV\frac{dV}{dz} = \pi a^2 (Sf_c' + N\rho V^2) \tag{10}$$

and integrating the right and left sides from V_1 to zero and $4a$ to P respectively giving

$$P = \frac{m}{2\pi a^2 \rho N} \ln\left(1 + \frac{N\rho V_1^2}{Sf_c'}\right) + 4a \tag{11}$$

In equation 11 every parameter is known except for the factor S. To determine the S factor Forrestal used equation 11 to calculate S based on experimental data. From the data a relation for S was developed as a function of the compressive strength, f_c', of the target material. Figure 5.3 gives this relation.
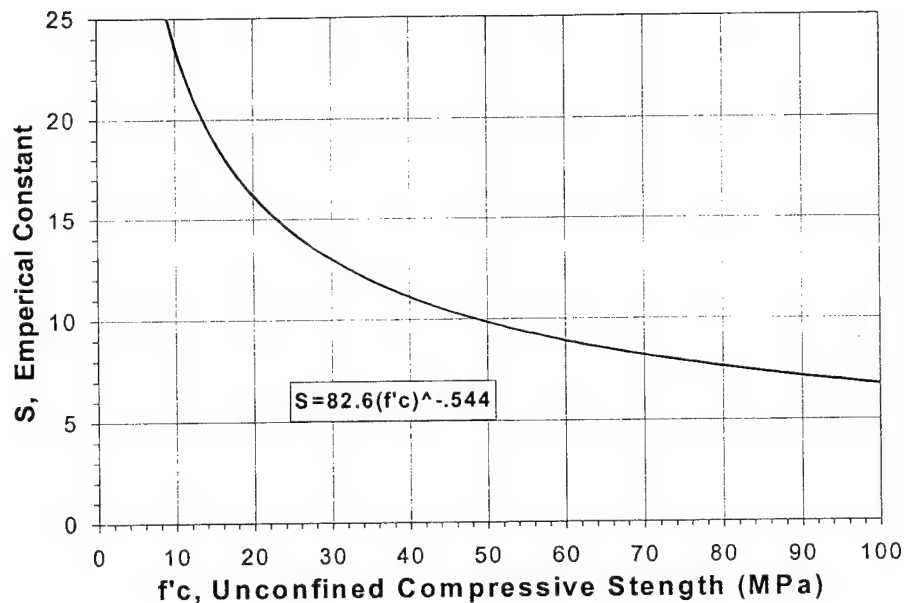
Figure 5.3. Empirically Determined Constant for Forrestal Concrete Penetration Model [8]

With this relation, a simple model can be used to calculate penetration of ogive-nose shaped projectile into concrete as long as the projectile geometry and velocity, and the target strength are known.

5.3.2   Extension of Model to Multiple Impact Penetration

The Forrestal single impact penetration model is convenient because it is based on parameters that are readily measured or known; projectile geometry, mass, and velocity; and target material unconfined compressive strength and density. The model is semi-empirical in nature due to a factor S that was originally determined from experimental data, but has been shown to be a function of the unconfined compressive strength of the target material. Observations made during the multiple impact penetration experiments, whose results were presented earlier, were similar to Forrestal's observations in the single

impact experiments. In both experiments, a crater was formed at the target surface, then the projectile tunneled into the material. Even upon subsequent impacts, the crater geometry remained unchanged, but the projectiles continued to tunnel. Also, the velocity range and target strength of the multiple impact experiments were similar to those used for the Forrestal Model development.

Due to these similarities, the Forrestal model was chosen as a starting point for empirically modeling the multiple impact penetration process. However, in the multiple impact experiments the crater depth was determined to be slightly deeper than in Forrestal's experiments. To account for this, equations 9 and 11 were recast using the transition from crater formation to tunneling as $z=5a$ as apposed to $z=4a$, there resulting equations were

$$V_1^2 = \frac{mV_s^2 - 5\pi a^3 S f_c'}{m + 5\pi a^3 N\rho} \tag{12}$$

$$P = \frac{m}{2\pi a^2 \rho N}\ln\left(1 + \frac{N\rho V_1^2}{S f_c'}\right) + 5a \tag{13}$$

Another slight difference noticed in the multiple impact experiments performed at the University of Rhode Island was the value of the S factor of the target material. Using the Forrestal relation shown in Figure 5.3, the S factor is 11.03. However calculating S using equations 12 and 13, and the initial impact penetration data for various velocities gives an average value of $S=15.47$.

At a given velocity, the initial projectile penetration into a target material can be predicted using the standard Forrestal empirical model. For a second impact at the same velocity, hitting the same point in the target, the projectile no longer sees virgin material. Now the projectile impacts the bottom of the previous projectile's tunnel region. Even

though the projectiles are seeing the same target material, its condition has been altered, so the scaling factor S, which modifies the unconfined compressive strength, must change with each impact. Since S is an empirically determined factor, it can be calculated using the reworked Forrestal model for each impact at the various velocities. Figure 5.4 show the back-calculated values of S for each test velocity as a function of shot number into the target.
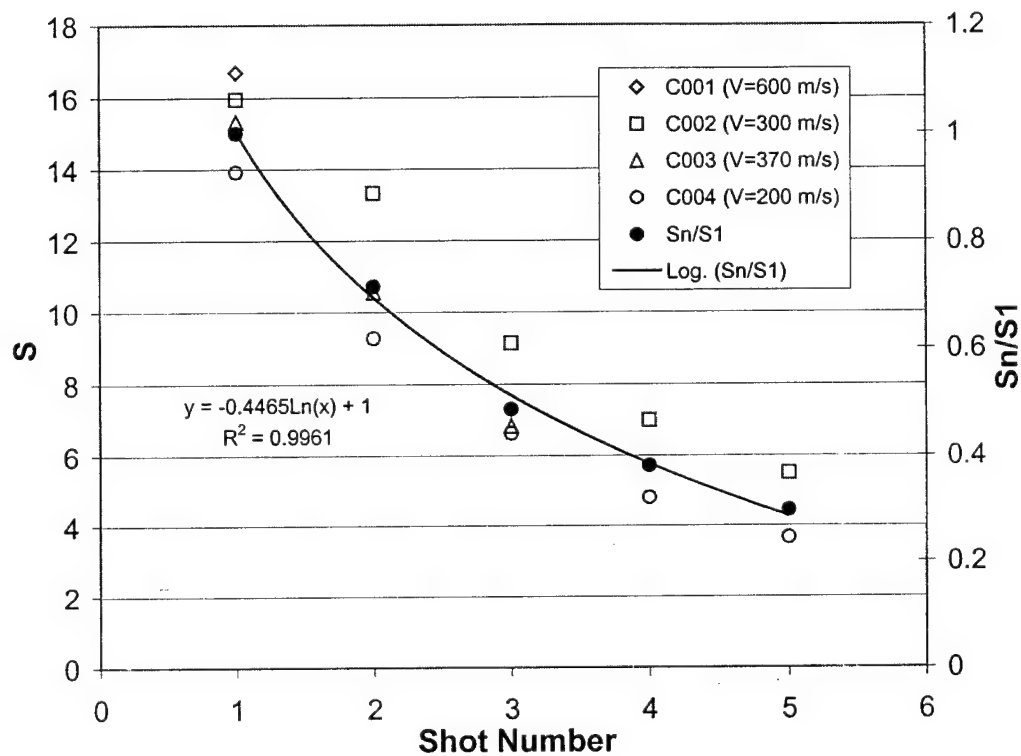
Figure 5.4. S as a Function of Shot Number for Multiple Impact Penetration of G mix Concrete

As shown, the effective S for a given shot number decreases as a function of

$$S_n = S_1(-0.4465\ln(n)+1)$$
(14)

where n is the shot number and S_1 is the factor for the initial shot into the undamaged target. Now, the penetration depth for each subsequent shot can be predicted using equations 12 and 13 by replacing S with S_n from equation 14 for the given shot number n.

5.4 MODEL RESULTS

Using the above method to calculate the penetration depth as a function of velocity for multiple impacts generates the family of curves shown in Figure 5.5. As shown the experimental data agree reasonably well with the predictions.
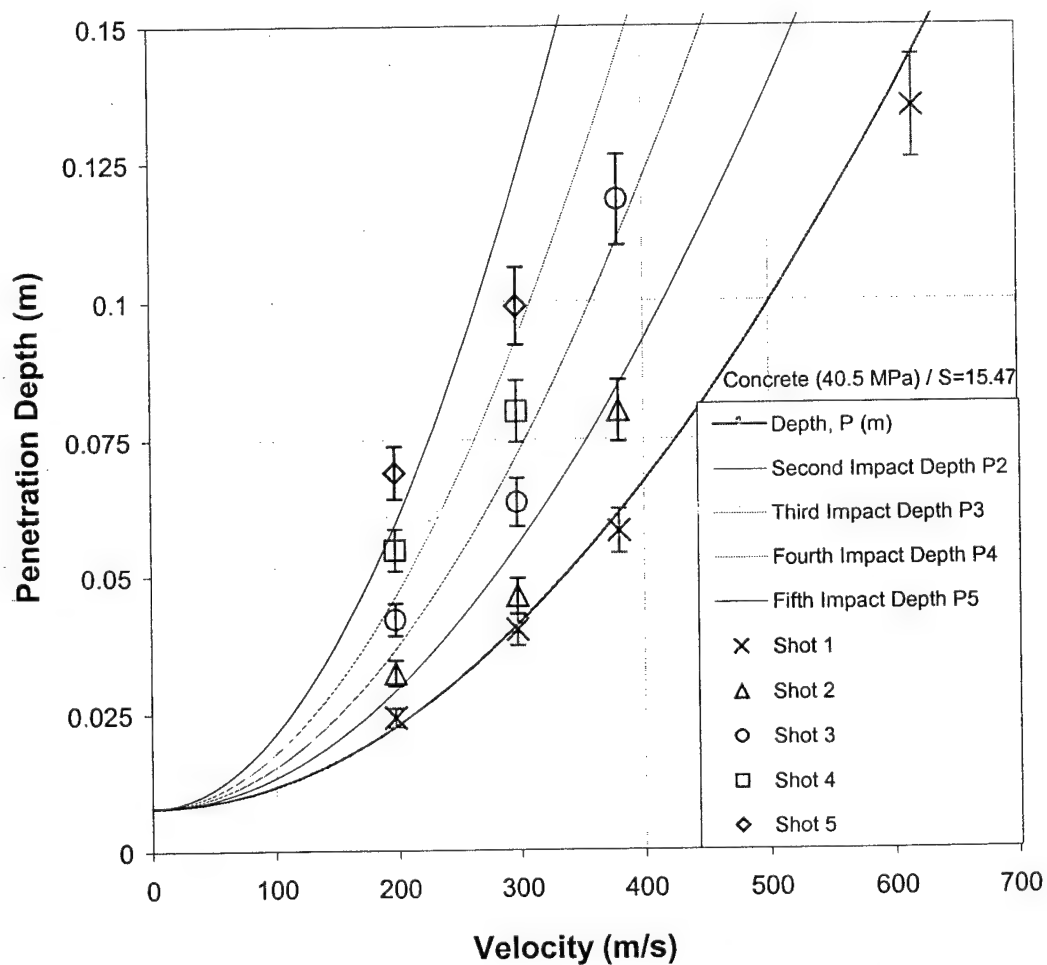
Figure 5.5. Multiple Impact Penetration Model Predictions

Another way to use the impact penetration model is to back calculate a degraded compressive stress in the target material as a function of shot number. As shown in Figure 5.6 this relation is identical to the relation for S shown in Figure 5.4.
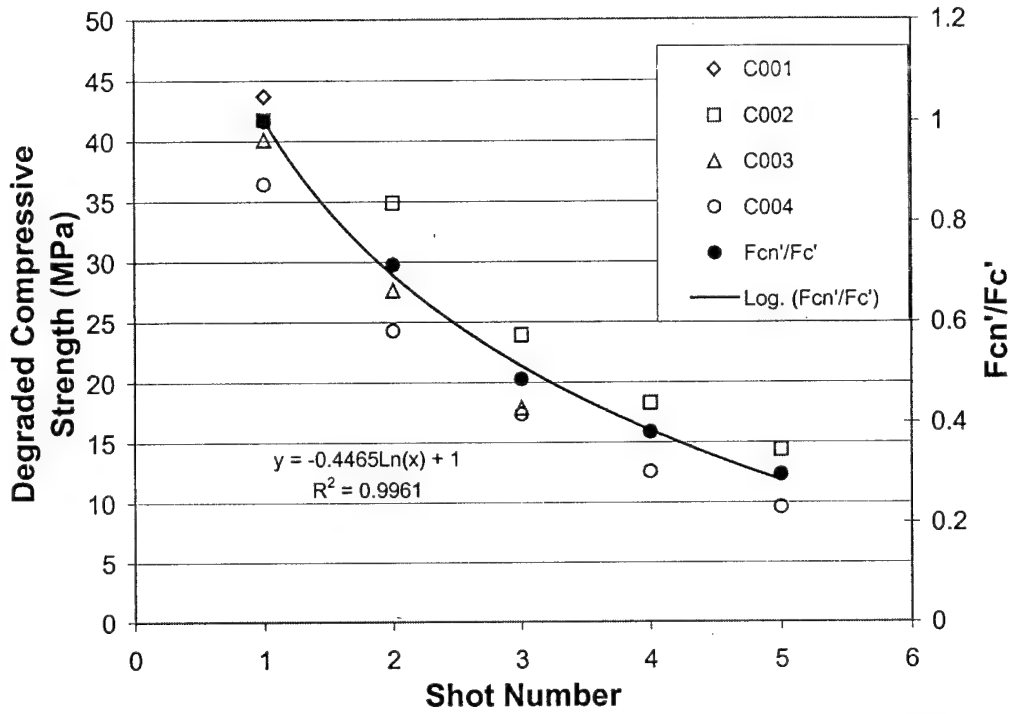
Figure 5.6. Degraded Target Compressive Stress, f'_{cn}, as a Function of Shot Number

With shot number, n, the compressive strength, f'_{cn} degrades with respect to the virgin unconfined compressive strength f'_c as

$$f'_{cn} = f'_c \left(-0.4465\ln(n)+1\right) \tag{15}$$

The family of curves shown in Figure 5.7 is generated by plotting and fitting the multiple impact penetration data versus this degraded compressive strength. This plot could be used to estimate penetration depth into a concrete target is a measure of its degraded compressive strength can be determined.
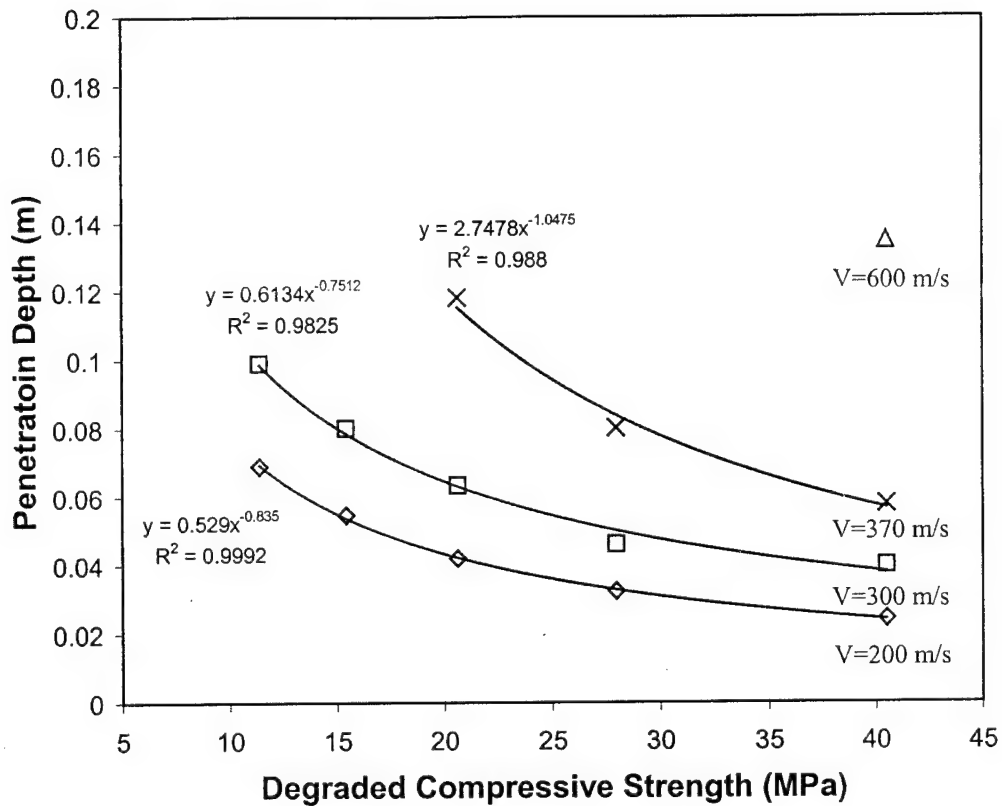
Figure 5.7. Penetration Depth into Concrete as a Function of its Degraded Compressive Strength

5.5 CONCLUSIONS

A multiple impact penetration study was conducted at the University of Rhode. Ogive-nose shaped projectiles were fired from a standard 30-06 rifle into a semi-infinite concrete target. In order to develop an empirical model that will predict the multiple impact penetration depth, the Forrestal single impact penetration model was modified fit the observations made during the study, and to account for the changing of the target for each subsequent shot. To do this, the target strength modifying factor, S, was empirically determined as a function of shot number. This relation was introduced back into the Forrestal model to predict penetration depth for the multiple impacts. As shown, the model aggress reasonably well with the penetration data.

82

5.6 REFERENCE

1. Forrestal, M. J., "Penetration into Dry Porous Rock", International Journal of Solids and Structures, vol. 22, no. 12, pp.1485-1500, (1986).

2. Luk, V. K. and Forrestal, M. J., "Penetration into Semi-Infinite Reinforced Concrete Targets with Spherical and Ogival Nose Projectiles", International Journal of Impact Engineering, vol. 6, pp. 291-301, (1987).

3. Bishop, R. H., Hill, R., and Mott, N. F., "Theory of Indentation and Hardness", Proceeding of the Physical Society, vol. 57, pp. 147-159, (1945).

4. Hill, R., "A Theory of Earth Movement Near a Deep Underground Explosion", Armament Research Establishment, Memo No. 21-48, Fort Halstead, Kent, UK, (1948).

5. Forrestal, M.J., and Luk, V.K., "Penetration into Soil Targets", *International Journal of Impact Engineering*, Vol. 12, pp. 427-444, 1992.

6. Forrestal, M.J., Altman, B.S., Cargile, J.D., Hanchak, S.J., "An Empirical Equation for Penetration Depth of Ogive-Nose Projectiles into Concrete Targets", *International Journal of Impact Engineering*, Vol. 15, No. 4, pp. 395-404, 1994.

7. Forrestal, M.J., Frew, D.J., Hanchak, S.J., and Brar, N.S., "Penetration of Grout and Concrete Targets with Ogive-Nose Steel Projectiles", *International Journal of Impact Engineering*, Vol. 18, No. 5, pp. 465-476, 1996.

8. Frew, D.J., Hanchak, S.J., Green, M.L., and Forrestal, M.J., "Penetration of Concrete Targets with Ogive-Nose Steel Projectiles", *International Journal of Impact Engineering*, Vol. 21, No. 6, pp. 489-497, 1998

APPENDIX A: SCHEMATIC OF VELOCITY SYSTEM FLIP FLOP CIRCUIT

STORAGE SCOPE MUST BE
SET TO TRIGGER ON RISING EDGE OF SIGNAL.
SET TIME BASE FOR 500 NS

OPERATION:
CONNECT GRID FOIL 1 AND 2. APPLY BATTERY
5V POWER. IF LED LIGHTS, DISCONNECT THE
CLIP FROM GRID 2, THEN RECONNECT GRID 2.
THE LED SHOULD BE OFF BEFORE FIRING GUN.
SET THE SCOPE TO TRIGGER. FIRE GUN.

WHEN GUN IS FIRED, GRID 1 'S BROKEN
CLOCK INPUT GOES HIGH, THE LOW TO HIGH
RISING EDGE CAUSES THE OUTPUT Q TO GO
HIGH. WHEN GRID 2 IS BROKEN, THE CLEAR
INPUT GOES LOW WHICH MAKES THE OUTPUT
LOW

GRID 2 IS NORMALLY AT GND, THIS KEEPS
THE INVERTER OUTPUT HIGH UNTIL THE FOIL
IS BROKEN. THEN INVERTER INPUT IS PULLED
HIGH AT 5V THROUGH THE RESISTOR
WHICH MAKES THE FLIP-FLIP CLEAR PIN LOW

84

APPENDIX B: BULLET RELOADING AND 30-06 VERTICAL GUN PROJECTILE IMPACT EXPERIMENTAL PROCEDURES

Reloading Procedures For The .30/06 Propellant Driven Gun

NOTE: Reloading can be a dangerous activity. Although the following instructions are a detailed, step by step process for reloading, they should not be used as a replacement for proper training by an experienced individual.

1. Install the .30/06 shell holder into the LEE press.

2. Install the Sizing Die. While holding the handle against the stop, screw the die in until it touches the shell holder, then release pressure from the handle and screw the die in an additional 1/4 to 1/3 of a turn maximum. Now while holding the die, tighten the lock ring.

3. Prepare your cases. Inspect your cases while lubricating them with LEE Resizing Lubricant. Discard all cases with split necks, indications of head separation, or other defects. Wipe on a thin film of lubricant with your fingers.

4. Place the lubricated case in the shell holder and raise the ram until the handle comes to a stop. Lower the ram and remove the case.

5. Prime the case using the LEE Priming Tool. Primers can be loaded into the round magazine with the flat side of the primer face down. Clean out primer pocket using the LEE Primer Pocket Cleaner. Place case into holder. Let a primer fall into the slot and then depress lever slowly to press the primer into the primer pocket.

6. Charge the case. To charge the case, care must be taken in choosing the amount of charge. One must know the mass of your projectile and the type of powder that will be used. Standard projectile charges can be found in Richard Lee's *Modern Reloading*. If you are not sure, do not guess. Overcharging can result in a blowback. Once the size of your charge is known, you can use the LEE Perfect Powder Measure. This will allow you to get the same charge each time much quicker than using the scale, although the scale is more accurate.

7. Place the case into the case holder and push the ram all the way up. Screw the Bullet Seating Die in until you fell it touch the case mouth. If no crimp is desired,

back the die out 1/2 turn. (Recommended: See Step 8 note.) If a crimp is desired, turn the die in 1/4 turn.

8.   Seat the bullet: Place a bullet on the case mouth and guide it into the die. Raise the ram to the top and withdraw. The knurled adjusting screw controls the bullet seating depth. Adjust to suit. Usually seating to the same depth as a factory round works fine. If you desire to crimp, be sure the bullet crimp groove is almost completely inside the case. Then screw the die in just enough to apply a good crimp. Attempts to apply excessive crimp will crush the case. For proper crimp, all cases must be trimmed to the same length. **Note**: For best utility and accuracy use the LEE Factory Crimp Die. You will never crush a case, no crimp groove is required and trim length is not critical.

NOTE: See the LEE Reloading Directions for pictures of all pieces of equipment.

30-06 Vertical Gun Procedure

Projectile:

1.   Calculate/estimate BLC-2 powder load from desired projectile velocity.(see attached plot for 15 gram steel projectile)

2.   Load projectile following standard reloading procedures mounted to window in gun lab. Record projectile mass without sabot prior to loading.
(1 gram = 15.432 grains)

Specimen/Target:

1.   Place specimen box, lined with plastic, on dolly.
Add thin layer (approx. 2-3 inches) of wetted sand on bottom of box.

2.   Load target into specimen box and adjust until level.

3.   Add wetted sand around target until flush with top (of target).

4.   Draw center axes, and incremental circles on target face.

5.   Cut square hole in plastic sheet slightly smaller than face of target.
Using duct tape, tape plastic sheet to face of target to isolate any sand from any shot rubble.

6.   Install laser sight assembly in action of gun, aligning scribe marks.
Turn on laser sight only when needed to conserve battery power.

7.   Move target into position, using laser sight to align with barrel of gun.

Velocity System:

1.   Apply mylar packing tape to back side of two (2) velocity screens for strength.
2.   Mount screens in holders (on specimen box cover).
        Screens must be held taut.

3.   Inspect wire connections on box cover.

4.   Install cover on specimen box with screw terminals facing upwards.
        Align screen center with gun barrel using laser sight.

5.   Connect screen (1) leads to upper screen terminals
        and screen (2) leads to lower screen terminals.

6.   Connect velocity circuit box to 6 volt battery and turn on power switch.
        Using terminals on top of Vel. Cir. Box, connect screen (1) then screen (2) until LED is off.

7.   Connect velocity circuit box BNC output to oscilloscope.

8.   Calculate time for bullet to travel distance between screens (2.887 in/0.07333m).
        Use assumed velocity as before.

9.   Set oscilloscope for appropriate time scale to capture full pulse of duration calculated above.
        Also set: 2V/div, 4V positive slope trigger level, and single data sequence capture.

10.   Test operation of velocity system, by removing terminals on top of Vel.Cir. Box

11.   Cover short section of stove pipe with cardboard and duct tape to act as blast shield. Place stove pipe over top velocity screen, being careful not to damage screen or wires.
        Ensure alignment with laser sight.

Test:

1.   Ensure gun is mounted securely on test box, and is plumb using adjustments.

2.   Close test box doors and lock.

3.   Remove laser sight assembly and set aside.

4.   Install bullet into gun action.

5.   Install and lock down bolt into gun action.

6.   Ensure velocity system and oscilloscope is set and awaiting trigger.

7.   Stand outside room with door closed, and pull trigger cord to fire gun.

Post Test:

1.   Record velocity pulse width, and copy data to disc.

2.   Open outside door to clear room of fumes.

3.   Remove bolt and spent shell from gun action.

4.   Open test box, and remove stove pipe.

5.   Turn off power to velocity system and disconnect from screen holders.

6.   Wheel   target   dolly   out   of   test   box   for   data   collection.

BIBLIOGRAPHY

ASTM C39, "Compressive Strength of Cylindrical Concrete Specimens"

Akers, S. A., Adley, M. D., "Constitutive Models Used to Simulate Penetration and Perforation of Concrete Targets", Proceedings of the 1996 American Society of Mechanical Engineers, Pressure Vessel and Piping Conference, Montreal, vol. 325, pp. 195-203, (1996).

Amirkian, A., "Design of Protective Structures", Bureau of Yards and Docks, Department of the Navy, report NP-3726, August (1990).

Backman, M. E. and Goldsmith, W., "The Mechanics of Penetration of Projectiles into Targets", International Journal Engineering Science, vol. 16, no. 1-A, pp. 1-99, (1978).

Ballistics Research Laboratory, "A Comparison of Various Materials in Their Resistance to Perforation by Steel Fragments, Empirical Relationships", Tech Report No 25, Aberdeen Proving Ground, MD, (1956).

Bardsley, W. E., Major, T. J. and Selby, M. J., "Note On A Weibull Property For Joint Spacing Analysis", International Journal of Rock Mechanics and Mineral Sciences & Geomechechanical Abstracts, vol. 27, pp. 133-134, (1990).

Bauer, A. and Calder, P. N., "Projectile Penetration in Rock", Canadian Department of Energy, Mines Resources, Proceedings of the 5th Canadian Rock Mechanics Symposium, Ontario, pp. 157-170, (1969).

Beth, R. A., "Concrete Penetration", National Defense Research Committee Report A-319, OSRD-4856, March, (1945).

Bernard, R. S., "Development of a Projectile Penetration Theory: Report 2, Deep Penetration Theory for Homogeneous and Layered Targets", US Army Waterways Experiment Station Technical Report, February, (1976).

Bernard, R. S. and Creighton, D. C., "Non-Normal Impact and Penetration: Analysis for Hard Targets and Small Angles if Attack", US Army Waterways Experiment Station Technical Report S-78-14, September, (1978).

Bernard, R. S. and Creighton, D. C., "Projectile Penetration in Soil and Rock: Analysis for Non-Normal Impact", US Army Waterways Experiment Station Technical Report SL-79-15, September, (1979).

Bishop, R. H., Hill, R., and Mott, N. F., "Theory of Indentation and Hardness", Proceeding of the Physical Society, vol. 57, pp. 147-159, (1945).

Blanton, T. L., " Effect of Strain Rates from 10^-2 to 10 1/sec. In Triaxial Compression Tests on Three Rocks", International Journal of Rock Mechanics and Mineral Sciences & Geomechechanical Abstracts, vol. 18, pp.47-62, (1981).

Brown, S. J., "Energy Release Protection for Pressurized Systems. Part II. Review of Studies into Impact/Terminal Ballistics", Applied Mechanics Review, vol. 39, no. 2, pp. 177-202, (1986).

Canfield, J. A. and Clator, I. G., " Development of A Scaling Law and Techniques to Investigate Penetration in Concrete", Naval Weapons Laboratory Report No. 2057, (1966).

Clifton, J. R. and Knab, L. I., "Impact Testing of Concrete", Cement and Concrete Research, vol. 13, no. 4, pp. 541-548, (1983).

Curran, D. R., Seaman, L., Cooper, T., Shockey, D. A., "Micromechical Model for Comminution and Granular Flow of Brittle Material Under High Strain Rate Application to Penetration of Ceramic Targets", International Journal of Impact Engineering, vol. 13, pp. 53-83, (1993).

Dutta, P. K., "A Theory of Percussive Drill Bit Penetration", International Journal of Rock Mechanics and Mineral Sciences, vol. 9, pp.543-567, (1971).

Frew, D.J., Hanchak, S.J., Green, M.L., and Forrestal, M.J., "Penetration of Concrete Targets with Ogive-Nose Steel Projectiles", International Journal of Impact Engineering, Vol. 21, No. 6, pp. 489-497, (1998).

Forrestal, M. J., "Penetration into Dry Porous Rock", International Journal of Solids and Structures, vol. 22, no. 12, pp.1485-1500, (1986).

Forrestal, M. J. and Luk, V. K., "Penetration into Soil Targets", International Journal of Impact Engineering, vol. 12, pp. 427-444, (1992).

Forrestal, M.J., Cargile, J.D., Tzou, D.Y., "Penetration of Concrete Targets", American Society of Mechanical Engineers, AMD-Vol. 171, pp. 9-16, (1993).

Forrestal, M.J., Altman, B.S., Cargile, J.D., Hanchak, S.J., "An Empirical Equation for Penetration Depth of Ogive-Nose Projectiles into Concrete Targets", International Journal of Impact Engineering, Vol. 15, No. 4, pp. 395-404, (1994).

Forrestal, M.J., Frew, D.J., Hanchak, S.J., and Brar, N.S., "Penetration of Grout and Concrete Targets with Ogive-Nose Steel Projectiles", International Journal of Impact Engineering, Vol. 18, No. 5, pp. 465-476, (1996).

Forrestal, M. J. and Tzou, D. Y., "A Spherical Cavity-Expansion Penetration Model for Concrete Penetration", International Journal of Solids and Structures, vol. 34, no. 31-32, pp.4127-4146, (1997).

Goldsmith, W., Sackman, J.L., and Ewert, C., "Static and Dynamic Fracture Strength of Barre Granite", International Journal of Rock Mechanics and Mineral Sciences and Geomechanical Abstracts, Vol. 13, pp. 303-309, (1976).

Heuze, F. E., "An Overview of Projectile Penetration into Geological Materials, with Emphasis on Rocks", International Journal of Rock Mechanics and Mineral Sciences and Geomechanical Abstracts, vol. 27, no. 1, pp.1-14, (1990).

Hill, R., "A Theory of Earth Movement Near a Deep Underground Explosion", Armament Research Establishment, Memo No. 21-48, Fort Halstead, Kent, UK, (1948).

Hudson, J. A. and Fairhust, C., "Tensile strength, Weibull's Theory and a General Statistical Approach to Rock Failure", The proceedings of the Southampton 1969 Civil Engineering Materials Conference (part II), Edited by M. Te'eni, pp. 901-914, (1969).

Jaeger, J.C. & Cook, N.G.W., Fundamentals of Rock Mechanics, 3rd Edition, Fletcher & Son Ltd, Norwich, Great Britain, (1979).

Kabo, M., Goldsmith, W., Sackman, J. L., "Impact and Comminution in Soft and Hard Rock", Rock Mechanics, vol. 9, pp. 213-243, (1977).

Kar, A. K., "Barrier Design for Torpedo-Generated Missiles", Transactions of the 14th International Conference on Structural Mechanics in Reactor Technology, paper J10/3, (1977).

Kennedy, R. P., "Effects of an Aircraft Crash into a Concrete Reactor Containment Building", Holmes and Navier, Inc., Anaheim, CA, July (1966).

Kennedy, R. P., "A Review of Procedures for the Analysis and Design of Concrete Structures to Resist Missile Impact Effects", Nuclear Engineering and Design, vol. 37, pp. 183-203 (1976).

Krajcinovic, D. and Silva, M. A. G., "Statistical Aspects of the Continuous Damage Theory", International Journal of Solids and Structures, vol. 18, no. 7, pp. 551-562, (1982).

Kou Shao-Quan, Lindqvist, P-A and Tan, Xiang-chun, "An Analytical and Experimental Investigation of Rock Indentation Fracture", The 8th International Congress on Rock Mechanics, Japan, F1-F4, (1995).

Kolsky, H., Proceedings of the Physics Society, B62, p. 676, (1949).

Li, G., Shukla, A. and Sadd, M., "The Effect of Damage on the Uniaxial Compression Behavior of Granite", Submitted to Journal of Engineering Mechanics, (1998).

Litewka, A., Bogucka, J., Debinski, J., "Deformation Induced Damage and Anisotropy of Concrete", Archives of Civil Engineering, vol. 42, no. 4, pp. 425-445. (1997).

Longscope, D. B. and Forrestal, M. J., "Penetration of Targets Described by a Mohr-Coulomb failure Criterion with a Tension Cut-Off", American Society of Mechanical Engineers Journal of Applied Mechanics, vol. 50, pp. 327-333, (1983).

Luk, V. K. and Forrestal, M. J., "Penetration into Semi-Infinite Reinforced Concrete Targets with Spherical and Ogival Nose Projectiles", International Journal of Impact Engineering, vol. 6, pp. 291-301, (1987).

Lundberg, B., " Penetration of Rock by conical Indenters", International Journal of Rock Mechanics and Mineral Sciences and Geomechanical Abstracts, vol. 11, pp. 209-214, (1974).

Malvern, L.E., Jenkins, D.A., Tang, T., and Gong, J.C., "Dynamic Testing of Concrete with the Split Hopkinson Pressure Bar", Proceedings of the Fourth International Symposium on the Interaction of Non-Nuclear Munitions with Structures, Panama City, Florida, pp. 296-301, April (1989).

Medrano, R.E. & Grills, P.P., "Weibull Statistics: Tensile And Bending Tests", Journal of American Ceramic Society, vol. 70, no. 10, pp. C230-C232, (1987).

Miller, M. H. and Sikarskie, D. L., "On the Penetration of Rock by Three-Dimensional Indentors", International Journal of Rock Mechanics and Mineral Sciences, vol. 5, pp. 375-398, (1968).

Nash, P. T., Zabel, P. H., Wenzel, A. B., "Penetration Studies into Concrete and Granite", American Society of Mechanical Engineers, Applied Mechanics Division, Presented at ASCE/ASME Mechanics Conference, vol. 69, pp. 175-181, (1985).

Nobile, L., "Damage Mechanics of Concrete", Engineering Fracture Mechanics, vol. 39, no. 6, pp. 1011-1014, (1991).

Pang, S. S., Goldsmith, W., Hood, M., "A Force-Indentation Model for Brittle Rocks", Rock Mechanics and Rock Engineering, 22, pp.128-148, (1989).

Pang, S. S., and Goldsmith, W., "Investigation of Crack Formation During Loading of Brittle Rock", Rock Mechanics and Rock Engineering, vol. 23, pp. 53-63, (1990).

Priest, S. D. and Hudson, J. A., "Discontinuity Spacing in Rock", International Journal of Rock Mechanics and Mineral Sciences and Geomechanical Abstracts, vol. 16, pp. 333-362, (1976).

Priest, S. D. and Hudson, J. A., "Estimation Of Discontinuity Spacing And Trace Length Using Scanline Curves", International Journal of Rock Mechanics and Mineral Sciences and Geomechanical Abstracts, vol. 18, pp. 183-187, (1981).

Paul, B. and Sikarskie, D. L., "A Preliminary Theory of Static Penetration by a Rigid Wedge into a Brittle Material", Transactions of the American Society of Mechanical Engineers, pp. 372-383, (1965).

Ratigan, J. L., "A Statistical Fracture Mechanics Approach to the Strength of Brittle Rock", Ph.D. Thesis, Univ. of California, Berkeley, California, (1981).

Robbins, B., "New Principles of Gunnery", London, (1742).

Robinson, H. P., "Terminal Ballistics", CPPA/B, NRC, (1941).

Rogers, C. O., Pang, S. S., Kumano, A., Goldsmith, W., "Response of Dry- and Liquid-Filled Porous Rocks to Static and Dynamic Loading by Variously-Shaped Projectiles", Rock Mechanics and Rock Engineering, vol. 19, pp. 235-260, (1986).

Rohani, B., "Analysis of Projectile Penetration into Concrete and Rock Targets", US Army Waterways Experiment Station, September, (1975).

Ross, C.A., Thompson, P.Y., and Tedesco, J.W., "Split-Hopkinson Pressure-Bar Test on Concrete and Mortar in Tension and Compression", ACI Materials Journal, vol. 86, No. 5, pp. 475-481, September-October, (1989).

Sen, Z. and Kazi, A., "Discontinuity Spacing And RQD Estimates From Finite Length Scanlines", International Journal of Rock Mechanics and Mineral Sciences & Geomechechanical Abstracts, vol. 21, pp. 203-212, (1984a).

Sen, Z., "RQD Models and Fracture Spacing", Journal of Geotechnical Engineering, American Society of Civil Engineers, vol. 110, pp. 203-216. (1984b).

Shockey, D. A., Curran, D. R., Seaman, L., Rosenberg, J. T., and Petersen, C. F., "Fragmentation of Rocks Under Dynamic Loads", International Journal of Rock Mechanic Science and Geomechanical Abstracts, vol. 11, pp. 303-317, (1974).

Shukla, A., Holloway, D. C., Wilson, W., "Influence of Nose Shape of Ceramic Projectiles on Damage in Granite Rock", Proceedings of the V International Congress on Experimental Mechanics, Montreal, pp. 433-438, (1984).

Silling, S. A., "Brittle Failure Kinetics Model for Concrete", Proceedings of the 1997 American Society of Mechanical Engineers, Pressure Vessel and Piping Conference, Orlando, vol. 351, pp. 263-268, (1997).

Sliter, G. E., "Assessment of Empirical Concrete Impact Formulas", Journal of Structural Division, American Society of Civil Engineering, May (1980).

Swan, G., "Fracture Stress Scale Effects For Rocks In Bending", International Journal of Rock Mechanics and Mineral Sciences & Geomechechanical Abstracts, vol. 17, pp. 317-324, (1980).

Tang, C.A., "Experimental Study Of Rock Failure", Ph. D thesis, Northeastern University, Shenyang, China, (1988).

US Army Corps of Engineers, "Fundamentals of Protective Design", Office of the Chief Engineer, Report AT1207821, (1946).

Vassallo, F. A., "Missile Impact Testing of Reinforced Concrete Panels", Calspan Report No. HC-5609-D-1, Calspan, Buffalo, NY, (1975).

Weber, P. and Saint-Lot, "A Statistical Model of Macroscopic Failure Under Compression", 5th International Congress on Rock Mechanics, Edited by A.A. Balkema, Rotteroam, A161-164, (1983).

Weibull, W., "A Statistical Theory of The Strength Of Materials", Royal Swedish Academy of Engineering Science Procedures, No.151, pp. 1-45, (1939).

White, M. T., "Effects of Impact and Explosion. Summary Tech Report of Div 2", National Defense Research Committee, vol.1, Office of Scientific Research and Development, (1946).

Wiederhorn, S. M., "A Probabilistic Framework For Structural Design", Fracture Mechanics of Ceramics, R. C. Bradt, D.P.H. Hasselman & F.F. Lange, (Eds.), Plenum Press, New York, pp. 197-226, (1981).

Xu, Y., Keer, L. M., and Luk, V. K., "Elastic-Cracked Model for Penetration into Unreinforced Concrete Targets with Ogival Nose Projectiles", International Journal of Solids and Structures, vol. 34, no. 12, pp.1479-1491, (1997).

Yazdani, S. and Karnawat, S., "Constitutive Theory for Brittle Solids with Application to Concrete", International Journal of Damage Mechanics, vol. 5, no. 1, pp. 93-110. (1996).

Young, C. W., "Depth Prediction for Earth-Penetrating Projectiles", American Society of Civil Engineers Soil Mechanics and Foundation Engineering, SM3, pp.803-817, (1969).

Young, C. W., "Equations for Predicting Earth Penetrating by Projectiles: an Update", Sandia National Laboratories Report, SAND 86-0013, (1988).

Zucas, J. A., "Impact Dynamics. Emerging Technologies in Aerospace Structures, Design, Structural Dynamics and Materials", Century 2-Emerging Technology Conference, San Francisco, CA, (1980).